Biomimetic leg design and passive dynamics of *Dolomedes aquaticus*

A novel approach to creating a compliant spider-like leg actuated by pneumatic air muscles

Jonah Belk

Te Whare Wānanga o Otāgo

A thesis

submitted in partial fulfilment

of the requirements for the degree of

Master of Science in Neuroscience

at the University of Otago, Dunedin
New Zealand
June 2020

Abstract

Spiders provide working models for agile, efficient miniature passive-dynamic robots. Joints are extended by haemoplymph (hydraulic) pressure and flexed by muscle-tendon systems. Muscle contraction in the prosoma leads to an increase in hydraulic pressure and subsequently leg extension. Analysis of body kinematics the New Zealand fishing spider, *Dolomedes aquaticus* indicates that elastic plates around the joints absorb energy from the ground reaction force when the force vector points backwards (i.e. would decelerate the spider's body in the direction of locomotion) and release it to provide forward thrust as the leg swings backwards. In addition to improving energy efficiency, this mechanism improves stability by passively absorbing energy from unpredictable foot-ground impacts during locomotion on uneven terrain. These principles guided an iterative design methodology using a combination of 3D modelling software and 3D printing techniques. I compared and contrasted compliant joints made of a variety of plastic materials. The final 3D-printed spider leg prototype has a stiff ABS exoskeleton joined by a compliant polypropylene backbone. The entire structure envelopes a soft silicone pneumatic bladder. FEA analysis was used to determine the ideal shape and behavior of the pneumatic bladder to actuate the exoskeleton. The spider leg can be flexed and contracted depending on the input pressure. To laterally actuate this pneumatic spider leg I designed and developed a fabrication system that uses vacuum injection molding to produce an integrated mesh sleeve/elastomer pneumatic actuator. I designed an apparatus to measure pressure and contraction of silicone and latex pneumatic muscles when inflated. I analyzed the non-linear pressure-contraction relationships of silicone versus latex pneumatic muscles, and also derived force-contraction relationships. From efficiency studies, both media muscles proved to be inefficient and the measuring apparatus needs to be more robust to prevent leaking air. The fabrication process still offers the possibility of a quick and efficient method of creating pneumatic muscles. A spider-like robot that implements these pneumatic muscles and pneumatic leg design could be used to explore the efficiency and stability of passive dynamic legged locomotion in spider-like robots.

Acknowledgements

Firstly, I would like to thank my supervisor Mike Paulin for his time and patience over the last two years. Thank you for originally offering me this research project, for softly guiding me when my thoughts or ideas were too far off track.

Secondly, thank you to "professor" Stu Borland, who filled the role of secondary supervisor during this project, dedicated a great deal of time to my project, gave me many ideas, and provided me with the tools necessary to complete the project.

To the staff and the students of the Zoology department- thank you. I understand why the Zoology's culture is the envy of across the University of Otago campus. As a neuroscience student, I was fortunate to be placed in a department where I was surrounded by people who are passionate about the natural world: to Paul Szyka, thank you for giving up your time to offer ideas of how to analyse biological resonance and for providing feedback on my work. To Nicky McHugh, thank you for accommodating my lab equipment needs. To Anne Ryan, thank you for giving up some of your glass syringes for hydraulic experiments. Last but not least, to Nat Lim, thank you for tolerating my invasion of your office space and for putting up with the loud noise.

To the many other people who I sought out or conversed with about this project, thank you for your time and advice. In particular thank you to Jason Hollis (Jtech Plastics, Mosgiel) for demonstrating injection moulding to me, and for donating your steel mandrils for casting.

To Stefan Reußenzehn and Kiri Pullar, while you are no longer at the University of Otago, your research was invaluable during this research process and provided the groundwork for many of my experiments.

Finally thank you to the rest of the masters students of room M120: Megha, Kim, Charlotte, John, Tessa, Aaron, Scott for the friendship, feedback, and innumerable hours of entertainment. Rowan Webster its been a blast over the last two years attending classes and sharing our little cubby-hole of an office. My deepest apologies if I contributed to any future asthmatic ailments due to all of

the plastic fumes I exposed you to ☺. I am glad I could share with you rage and frustration every time the 3D printer decided to throw a mechanical fit.

Last but not least, thank you to my family for their love and support over the last two years.

Table of Contents

List of Figures

List of abbreviations

3D	three dimensional
A	area
ABS	acrylonitrile butadiene styrene
BRep	boundary representation
C	celsius
Cos	cosine
Cox	coxa
ΔPP	change in pressure
ΔLL	change in length
D_o	initial diameter
DOF	degree of freedom
E	exponential
FDM	fusion deposition modelling
FEA	finite element analysis
Fem	femur
F_{pp}	pulling force
F_{t}F	tension force
GPa	gigapascal
ID	inner diameter
J	joule
Kg	kilogram
L1	first leg leg
L2	second left leg
L3	third left leg
L4	fourth left leg
L_1	initial length
L_2	final length
M	mass
MKM	mckibben muscle
MPa	megapascals
OD	outer diameter
P	pressure
P_o	initial pressure
P_1	final pressure
π	pi
PLA	polylactic acid
PP	polypropylene
r	radius
R1	first right leg
R2	second right leg
R3	third right leg
R4	fourth right leg
SLA	Stereolithography
SE	standard error
SLIP	Spring loaded inverted pendulum
Tar	tarsus
θ	angle
Tib	tibia
Tro	trochanter
ToF	time of flight sensor
V	volume
W	watts
DPS	differential pressure sensor

1 Introduction

1.1 Biorobotics and Biomimicry

Nature is arguably the best teacher. Human beings have instinctively drawn inspiration from biological organisms to create, design, and improve on technology. Beginning with the wheel, human civilizations have designed technologies that improve locomotion to transport loads across large distances with minimal energy expenditure. Often technological developments were inspired by solutions found in nature and consequently there has been a reciprocal mimesis of comparing organisms as analogous to machines, and vice versa. Aristotle famously highlighted this dual-relationship, claiming that technology imitates nature but described nature in terms of human technology (Bensaude-Vincent 2011). This tendency to view the natural world from a mechanical lens was carried into the 18th century with philosophers such as Renee Descartes claiming that animals are like machines or automata incapable of feeling pain (Harrison 1992). Manmade machines took on a new role in the early 20th century when the word "robot" was coined. "Robot" was first introduced in Carl Kapek's 1920 play "R.U.R: Rossum's Universal Robots". The Czech word *robota* literally translates as 'forced labor' (Margolius 2017). True to their etymological origins, robots of varying forms have been constructed for convenience, exploration, industry, and understanding biological systems. The acceleration of technological development reached a new milestone with the advent of cybernetics and bionics in the 1950's (Bensaude-Vincent 2011). In succeeding decades, it can be argued that roboticists have depended more on mathematics, electronics, and computer science to design and create industrial robots. However, as researchers investigate machine learning and autonomous robots at an accelerated rate in the last decade, biological organisms have again become a source of inspiration for design because of their adaptability to environmental niches (Meyer and Guillot 2008). Design that mimics nature is termed "biomimicry" and takes into consideration the structural properties and principles of locomotion of the specific biological model (Pauslon 2004).

Biomimetic approaches have recently proven successful in developing autonomous vehicles (Altendorfer et al. 2001; Pauslon 2004; Fish and Lauder 2006; Sfakiotakis and Tsakiris 2007) Autonomous vehicles are particularly important for exploring hazardous or remote environments.

Consequently, to navigate these environments, we create autonomous robots. These robots have integrated mechanical and structural solutions inspired by biological organisms that have evolved mechanisms over successive generations to take advantage of their ambient environment.

In nature, being energy efficient is key to locomotion. Locomotion is a dynamic interplay between internal and external forces and can be viewed as an engineering system. Like biological organisms, engineers seek to decrease extraneous energy expenditure in robotic models by modelling and including biological facets into their hardware (Gao et al. 2019). By including these naturally occurring energy-saving principles these robots, biomimetic robots, can be used as integrative models for understanding an organism's biology and behavior. As an example of this dual relationship, the Wright brothers observed birds to fully understand how air moving over a curved surface created lift, eventually leading to the brothers' first successful flight at Kittyhawk (Bereiter 2009). Robert Full termed this synergy between two disciplines, in this specific case biology and robotics, as "biomutualism" – each discipline reciprocally advancing the other one (Full 2009). In one example, Robert Full's lab designed a robotic gecko to study the Van der Waals forces in a gecko's feet that allowed it to climb vertical surfaces(Full 2009). Unintentionally, during their research, Full's lab surprisingly discovered the importance of the gecko's tail in almost all locomotor activities from climbing, to jumping. Biologists had not considered the importance of the gecko's tail in kinematics before, and both the robotics and biology fields were advanced by the discovery (Full 2009).

Developing a biorobot is a bidirectional process of learning about an organism's physiological behaviors. When reverse-engineering an animal's design constructing biorobots can afford an "understanding by building" approach (Pfeifer and Scheier, 2007). Fish, cockroaches, salamanders, snakes and cats are a few examples of organisms that have been studied and whose locomotor abilities have been replicated in robots (Jayaram and Full 2016; Neveln et al. 2013; Ijspeert et al. 2007; Spröwitz et al. 2013). Flapping, climbing, jumping, swimming, and limbless locomotion such as slithering are a few of the locomotor behaviors that have been mimicked in robots. In unstructured environments, multi-legged legged robots that have two, four, six, or more legs move more dexterously over uneven surfaces compared to tracked or wheeled robots (Gao et al. 2019). Kinematic analysis and simulations have led to quadruped and hexapedal robot

development. On uneven terrain, having an increased number of legs, and additional degrees of freedom leads to increased maneuverability. Robots such as Boston Dynamics' "Big Dog", Tokyo Institute of Technology's Kumo-I and Titan series, and BioRob's Cheetahcub are a few well-known quadrupedal robots examples (Raibert et al. 2008; Hirose and Kato 2000; Spröwitz et al. 2013). However, many of these polypedal robots are energy inefficient. There is a disparity between the cost of transport (COT) of animals and the modelled robots, of a similar mass such as Big Dog and the Honda's bipedal ASIMO robot. Consequently there have been research attempts to create energy efficient multi-legged robotic locomotion employing passive dynamics and elastic actuators demonstrated in the MIT cheetah (Seok et al. 2013)

Biorobots can be used as scientific tools to test hypotheses about the underlying interactions of body control, and environment. From an external view the principles of animal locomotion may appear simple, but this simple movement is complex and determined by interactions between the nervous system, musculo-skeletal system, and tissues. These move in a high-dimensional and non-linear fashion creating a difficult modelling problem. In addition, modelling biomechanics must investigate how the body interacts with and changes with the external environment (Ijspeert 2014).

1.2 Intelligent Design: Interplay between the Nervous System and Biomechanics

Selective pressures by the environment and predators shaped the evolution of nervous systems (Monk and Paulin 2014). Even though nervous systems have evolved over millennia, they are still energetically expensive and an organism must adjust its behavior to optimize energy expenditure. It is a misconception to believe the nervous system is solely responsible for adjusting adaptive behavior, behavior that advances survival and reproduction. Instead, an interplay between an organism's nervous system, biomechanics, and its environment is more a holistic illustration of processing input information to optimize future actions (Chiel and Beer 1997). Dynamic feedback loops are formed as environmental factors are translated to sensory information, directly influencing both body kinetics and the nervous system; in turn the body adapts its behavioral frequency to the oncoming stimuli.

Locomotion is often mediated by central pattern generators (CPGs), groups of neural circuits that are responsible for rhythmic neural activity and independent of environmental input. The rhythmic patterns of CPGs, in both vertebrates, and invertebrates can be shaped by afferent sensory feedback leading to changes in behavior. Examples of activity-controlled CPGs include breathing, chewing, walking and swimming (Ijspeert 2008; Delcomyn 1980). Independent of these activities, an organism's body has a natural oscillating frequency (Ahlborn et al. 2006). CPGs rhythmic output can align to external behavior, specifically the natural mechanical frequency of the body, to produce what is termed "resonance entrainment" (Tytell et al. 2011). Resonance entrainment is an adaptive control method to decreases energy expenditure.

Resonance entrainment can be simulated in a robotic model by coupling mechanical behavior and artificial neural networks such as neural oscillators. These neural oscillators simulate how groups of neurons rhythmically fire. Further, these generated oscillating neuronal models can be incorporated into biomechanical simulations of a body, also known as neuromechanical models (Ijspeert, 2008). Some of these tested neuromechanical models include a swimming fish and a walking salamander (Ekeberg 1993; Ijspeert et al. 2005). It is obvious when robotic movement is dependent on the control of a neural net, however another piece of the locomotion puzzle is still missing – the design of the musculoskeletal system. Articulated movement not only stems from an understanding of the nervous system but the intelligence of mechanical design of the musculoskeletal system as well (Blickhan et al. 2007).

Designing a computational model of a mechanical locomotory system may seem simple, but as the number of multi-joint appendages increase so do the degrees of freedom and the complexity, making it difficult to apply a computational model. Compounding this, animals demonstrate kinematic redundancy and actuator redundancy, in that they have more muscles and mobility than needed to complete a given behavior (Fish and Lauder 2006). Because of this redundancy, animal biomechanical models can be simplified. Full and Kodetschik (1999) proposed a mechanical reductive template-anchor model that depicts the motion of a body in its simplest form with minimal variables. The model reveals the basic principles about the high-level of control strategy needed to govern a given animal's locomotion. Muscles, bones, neurons, and tendons are treated as entire entities, reducing physiological symmetries and redundancies. First, a template is built

that predicts the pattern of goal behavior. Secondly, an anchor, a more complicated dynamic system, is overlaid on the template. The relationship between the template and anchor offers a more complete understanding of the hypothesized neuromechanical control of the moving organism (Full and Koditschek 1999). The methodology supporting the template-anchor framework based on mathematical models that use this reductionist approach to describe the duty factor and ground force pattern of walking (Alexander 1991; Cavagna et al. 1977).

1.3 Energetics and Kinematics of Locomotion

When analyzing locomotion, it is natural to begin with humans as a base model because the human gait can be broken down simply into two gait forms: walking and running (Alexander 1996). Each gait is energetically efficient for a specific speed range and terrain profile (Halsey 2016). When considering the conservation of energy of transport of an animal, one may apply a known simple mechanical system. In the case of locomotion for most vertebrates, one employs the inverted pendulum analogy (Cavagna et al. 1977). The swing arm which pivots from a fixed point can be analogous to appendages, and the ball, and organism's center of mass. The pendulum is a useful model as it represents the *ideal* conserved energy system where there is an equal trade of gravitational potential energy to kinetic energy, and where the recovery energy of each revolution, or swing is close to 100%. Human bipedal locomotion can be compared to two inverted pendulums with a fixed point close to the center of mass, in the lower abdomen. From this inverted pendulum viewpoint there are elements of potential, kinetic and elastic energy due to muscle contraction, tendon tension, and gravity (Saibene and Minetti 2003). It is thought that muscles may not be key in energy expenditure during steady locomotion, instead, the oscillations between potential and kinetic energies are stored and recovered in the tendons and ligaments (Biewener 2003). Similarly, mechanical work done by the body can be broken down into external and internal work. External work can be described as the work done to move and accelerate a body in space while internal work is the work done accelerate body appendages in relation to the center of mass. During running, the impact of the legs on the ground to keep the body moving is an example of external work while the movement of the arms is viewed as internal work (Saibene and Minetti 2003). A previous study refined the bipedal model of locomotion into a simple spring-mass system governed

by three variables: stride frequency, the duty factor, and the shape of the ground reaction force (Blickhan 1989). The "duty factor" is the proportion of the stride duration during which the foot is in contact with the ground. The point of this study was to demonstrate that in humans, there is a particular speed where it mechanically and metabolically "cheaper" to run than to walk. Also noted in some studies was that while total external work accurately represents the work done by muscles while walking, the total work cannot be attributed to muscle output alone as the storage and release of elastic energy from the tendons and ligaments is greater at high speeds. As the body accelerates, the body must transition from one gait to another as the centrifugal force of the center of mass becomes greater than the gravitational force leading to loss of ground contact (Saibene and Minetti 2003). At a particular resonant frequency of motion, energy consumption is at a minimum and particular resonances can change in response to a change in speed. For example, during walking there is an ideal frequency of leg turnover that minimizes the amount of energy consumed to place one foot in front of the other. To accommodate a higher walking speed, it becomes necessary to have a faster leg turnover, but this may be more energetically inefficient compared to switching over to a running gait. For each form of locomotion, whether walking or running there is one natural frequency that requires a minimal amount of energy input but a high energy efficiency within a system (Ahlborn et al. 2006).

If body components such as a muscle and tendons can be likened to a spring, then concentric, eccentric, and isometric contractions of the muscles can lead to a storage or dissipation of elastic energy. As an example, on impact with the ground during running, there is a concentric contraction of the calf muscle and the Achilles tendon lengthens, storing elastic energy. This elastic energy is converted into kinetic energy and passes into the ground as a force and is further translated into forward momentum. As a result, the leg swings back and there is flexion and the knee bends. If the leg were thought of as a pendulum in walking, tangential gravitational energy is converted to kinetic energy as the leg swings down from a given height and overshoots the ground, ignoring the absence of friction. The leg would continue on an upward trajectory behind the body but is resisted by the torque from the coupling of the hip joint and surrounding muscles (Ahlborn et al. 2006). Considering the elasticity, the compression and rebound, of ligaments and muscles in a walking gait, the inverted pendulum model can be built on to include a spring. The added spring allows for more energy storage, shock tolerance, and control compared to the inverted model. This

model is referred to as a spring-loaded inverted pendulum (SLIP) (Full and Koditschek 1999). The SLIP model has been applied to robots to create bouncing mechanical systems that are driven by elastic actuators (Raibert 1986).

In an optimal energy efficient mechanical system, length of an appendage is proportional to a particular resonance frequency. The shorter overall length of an appendage when swinging, the higher the resonant frequency of a system; the opposite is true for longer appendages. As the stride frequency increases it is metabolically more efficient to switch from walking to running. As one begins to run, the flexion in the knee provides a shorter overall appendage length, as a proportion of the whole leg, and this results in a higher resonance frequency. However, the leg does not have the majority of its mass centered at the foot but is distributed in the muscles throughout the leg. By minimizing the amount of mass in the distal leg segments, such as large muscles, there is an increase in the resonant frequency as there is less rotational inertia to oppose the swing phase (Ahlborn et al. 2006).

Often people take an anthropocentric view analyzing other species' gaits by simplifying individual complex mechanics with respect to human bipedal locomotion. A classic example of this anthropocentric method is deconstructing the horse's gallop, which can be simplified as two bipedal running cycles out of phase (Nentwig, 2013). At higher speeds, such as galloping, running, or hopping in the case of the kangaroo, elastic energy stored in the ligaments and tendons plays an important role in energy recovery returning up to 93% of the energy stored (Biewener, 2003) With addition of another pair of legs, the six-legged cockroach operates with an alternating tripod manner, the front right leg, middle left leg, and hind right leg move in unison over half a walking period. While each leg of a quadruped produces a similar ground reaction force pattern, the legs of a hexapod produce their own individual ground reaction pattern. As a comparison, each tripod movement of a hexapod is analogous to the single leg movement of a bipedal animal (Full et al. 1991). In an ideal system such as a pendulum, 100% of energy would be recovered but in one particular study where the kinematics of the cockroach were analyzed, it was discovered that there was only 15.7% of energy recovered (Full and Tu 1990). The conservation of energy in these animal systems necessitates the need for study and incorporation of passive dynamics into robots.

1.4 Passive Dynamics: Efficient robots

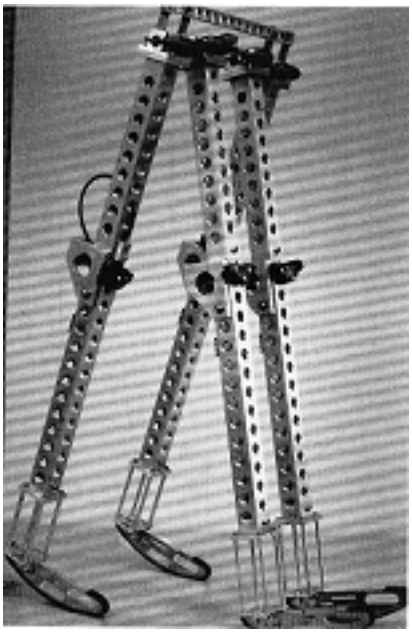

Figure 1.1 McGeer passive dynamic walker:
Four-legged "bipedal" robot that walks without the aid of actuators (McGreer 1990).

Since the mid-1980's, roboticists such as Tad McGreer investigated making robots more dynamic rather than static. Static robots as McGreer described, require the machine to maintain static equilibrium throughout motion compared to dynamic machines which are modelled closer to the biological model allowing them to move faster and self-correct their gaits (McGeer 1990). The dynamism is also in reference to the passive dynamics of the modelled system where there is an efficient cyclic exchange of kinetic to potential energy, reducing the given input of energy close to zero. Mechanical design alone can lead to 100% efficient gait in an idealized model with no brain or muscles (McGreer 1990; Chyou et al. 2011). Passive walkers have been built by other research groups such as the Cornell Robot (Collins and Ruina 2005). The primary form of energy dissipation in robots is when the foot strikes the ground, and the braking of actuators termed negative work. The Cornell biped robot only applies positive work, extending the ankle and leg reducing the overall power input. Similarly, the MIT Learning Robot has limited actuation, but uses reinforcement learning, simple feedback, to tune its gait (Collins 2005). Depending on the animal system in question, for a given number of joints in an appendage and its length, there is a particular frequency that the system optimally cycles through (Ahlborn et al. 2006). For example, the optimal speed for a bipedal walking gait is 1.11 m/s^{-1}, and with an increase in speed it would

be more efficient to change to a running gait (Saibene and Minetti 2003). By building a robotic system according to the passive dynamics, inherent in the specific biological model in question, one does not need to worry about speed control, direction, or the driving force of the machine (McGeer 1990).

1.5 Study Model: The Nurseryweb spider *Dolomedes aquaticus*

There has been little research dedicated thus far to the study of passive dynamics in spiders (Sensenig and Shultz 2006; Moya-Laraño et al. 2008; Biancardi et al. 2011). Cyclical changes of the harvestman's, commonly known as the daddy longlegs, center of mass indicates there is a net interchange of kinetic and potential energy during the harvestman walking gait cycle. In addition to this noticeable conservation of energy, SLIP and LLS (Lateral leg spring) models outlined by Full and Koditschek (1999) accurately describe the kinematics and locomotion patterns of the harvestman (Sensenig and Shultz 2003). However, in comparison to other smaller wandering spiders, ground-based spiders, the Harvestman has significantly longer legs relative to body size. Different leg to body to proportions could lead to differing passive dynamics. Moya-Laraño et al. (2008) did specify that pendulum mechanics were observed in 105 species of spiders, but that it depended on whether they lived in webs and were inverted, or were ground-based. Preferential habitat, in a web or on the ground, dictated body to limb ratios with web-based spiders having disporpotionately longer legs than ground-based spiders. Whether bridging is energetically more efficient than wandering remains to be determined. Central Pattern generator activity has been studied in six-legged insects extensively, but little in spiders. Even within the hexapedal research there are still gaps in knowledge of the neural mechanisms that drive the insect gait (Bidaye et al. 2018). Simple Computational CPG models that integrate sensory feedback to entrain to an animal's body mechanical resonance have been studied, but none to date have been applied to spiders (Zheng 2006).

Dolomedes species are genus of large spiders endemic to New Zealand that spin nursery webs (Goyen 1887). Dolomedes species in Australia, South Africa, and North America have been reported to prey on a variety of organisms including salamanders, fish, and tadpoles (McKeown

1935; Kaston 1965). Among New Zealand *Dolomedes* species, *Dolomedes aquaticus* is found in stony areas of braided streams. *Dolomedes aquaticus* is an opportunistic feeder, but its primary prey, adult aquatic insects are active at night. *Dolomedes* species are recognized as hunting spiders, but specifically *Dolomedes aquaticus* can be found waiting passively for prey flying or traveling by the water's edge. Mechanoreception appears to be the primary method of detecting prey, over visual and chemical stimuli from prey. It is believed the front legs are important in sensory perception, anticipating the vibrations created by prey both on water and land (Forster and Forster 1973). Its ability to locate, move, and seize prey in multiple media up to 40cm away, even in fast-flowing water, indicates *Dolomedes aquaticus'*s ability to move rapidly (Williams 1981). It is a model of bipedal locomotion on compliant legs. The ability to move rapidly over large distances indicates that these spiders exploit dynamic stability. The front legs would serve a dual-purpose of sensing prey, but also obstructions while moving. To preemptively modify gait patters according to oncoming ground perturbations, serves to minimize energy loss and increase locomotor agility (Monk and Paulin 2014; Pullar and Paulin 2018; Chyou et al. 2011). The forelegs of Dolomedes spiders have also been hypothesized to be specialized in tactile sensing and out of phase with the aft six legs, indicating Dolomedes adopts an alternating tripod gait, like other hexapod insects (Pullar and Paulin 2018).

Spiders within the *Dolomedes* genus are a good study group of animals for robotic design because of their ability to adapt and specialize in most environments. Their unique morphology and physiology makes them extremely agile, capable of jumping, running and burrowing. Rather than muscle-driven leg articulation, the flexion and extension of leg joints is forced through a hybrid system of extensor muscles and the hydrostatic pressure of hemolymph (Reußenzehn 2010; Sinha et al. 2017). This hydraulic system has been modeled in several studies to develop a powerful biomimetic fluid actuator for robots and other biomechanical applications (Menon and Lira 2006; Nentwig 2013; Landkammer et al. 2016; Sinha et al. 2017). However, even though there has been interest in developing individual fluid actuators, many of the polypedal robots produced today rely significantly on servo-motor driven movements, reflective of the pervasive static movement and lack of dynamic movement referred to by McGreer (McGreer 1990). There have been studies into the passive dynamics of spider gaits and the energy conservation; one of the specific studies looked at the comparison of applying spring-loaded inverted pendulum models to the suspended

pendulum model for different spider gaits (Sensenig and Shultz 2006). Regardless, the findings from Sensing and Shultz need to be applied to spider robotic models for the following reasons: 1) robots can be used as a platform for other neural system simulations. 2) natural rhythmic limb oscillations and efficient recovery of energy from each step, which results in less processing power for the robot. 3) fewer external motors on limbs result in lighter appendages and less power.

In Stefan Reußenzehn's 2010 thesis, he quantified the joint-angle characteristics of *Dolomedes aquaticus,* a species of fishing spider endemic to New Zealand. He outlined the importance of studying the mechanical design of the Dolomedes legs to fully understand a spider's locomotive abilities. Reußenzehn assessed the differences between the joint-angle relationships of different segments based on leg position (Reußenzehn 2010). As mentioned the Dolomedes species' dynamic stability when running makes it a prime candidate for studying its passive dynamics. In order to understand the underlying principles of its passive dynamics, it is necessary to investigate the mechanical design of its legs.

1.6 Objectives of this Study and thesis outline

An understanding of the mechanical design of animals appears to lag behind the development ofartificial neural nets for robotic control. This gap has resulted in robots that are energy-inefficient (Seok et al. 2013). As robots gain more autonomy there is an associated cost of increased energy consumption, manifested as a requirement for more powerful batteries. Computation energy needs dedicated to robotic control can be reduced if the "mechanical intelligence" of the modeled organism is understood. In other words, a shift in design from *statically* stable robots to *dynamically* stable robots will lead to more computational space dedicated to autonomy. In this study I have built on Reußenzehn's (2010) previous work, analyzing the mechanical design of *Dolomedes aquaticus* and creating a passive dynamic walker that embodies the passive dynamics of the biological model, *Dolomedes aquaticus* according to the joint/angle relationships which he identified.

Objectives of this study

- Design and fabricate a leg that is compliant according to the passive qualities of a Dolomedes leg
- Develop a method of actuation that takes advantage of the compliance of the spider leg
- Design a passive dynamic walker that is minimally actuated

2 Biomimetic Spider Leg

2.1 Introduction

2.1.1 Fluidic Actuators in Robotics

Industrial robots often have joints that are articulated by heavy electric motors. This leads to increased joint mass, increased energy expenditure, and increased inertia (Landkammer et al. 2014). In comparison, pneumatically controlled robots are lightweight and compliant lending to safe human-robot interactions (Kim et al. 2018). Pneumatics enable robots to move with greater control, dexterity and flexibility compared to conventional mechanical industrial robotic systems. Because of these favorable properties, fluidic actuated robotic systems have been incorporated into medicine and industry (De Greef et al. 2009; Blanes et al. 2014; Belforte et al. 2014; Surentu et al. 2007).

Industrial robotic systems are often inspired by biology. Biological systems are efficient and utilize natural mechanisms which are compliant but also elastic (Dickinson et al. 2000). Muscles, tendons, and other connective tissues are examples of biological actuators that exert energy on the external environment yet act like natural elastic springs, dampening ground-impacts and reabsorbing energy during movement (Hill 2018, 1938; Klute et al. 2002). Animals have taken advantage of these tissues allowing them to navigate complicated environments; thus they have inspired designs of engineers and roboticists. For example, the spider's multi-segment compliant leg has become a source of inspiration for designing energy-efficient actuation systems (Landkammer et al. 2014; Nentwig 2013; Sprowitz et al. 2017).

2.1.2 Spider Biology and Biomechanics

The spider body can be subdivided into two main parts, the anterior cephalothorax and the posterior abdomen. All eight legs are attached to the cephalothorax, anterior to the abdomen. Each spider leg consists of seven different segments: Coxa, Trochanter, Femur, Patella, Tibia, Metatarsus and Tarsus. Each segment (also called podomeres) are hollow cylinders connected by cuticle joint membranes. Spiders have an open circulatory system where haemolymph, analogous to blood in vertebrates, flows freely throughout their bodies and their legs (Figure 2.1). In all legs, podomeres

are innervated by longitudinal muscles which, when contracted, cause flexion and extension in most joints (Foelix 1983). However, the femur-patella joint, and the tibia-metatarsus joints are exceptions to this physiological paradigm, and lack extensors thus relying on hydraulic pressure of pressurized haemolymph for extension (Petrunkevitch 1909). Thus, the femur-patella joint and tibia-metatarsus joints could be used as a model for biological pneumatic actuators.

From a mechanical design perspective the spider's physiology and dimensions are relatively simple: Spider legs are long and slender with most of the muscle mass located proximally near the prosoma to decrease rotational inertia during the swing phase of locomotion (Blickhan and Barth 1985). Each joint of the spider leg has minor differences in degrees of freedom and have consequently been likened to different mechanical joints. The body coxa-joint, coxa-trochanter joint, trochanter joint, and metatarsus-tarsus joints can all be modelled as ball-and-socket-joints with multiple degrees of freedom. The musculo-hydraulic actuated femur-patella joint, and the tibia-metatarsus have been likened to hinge joints with a single degree of freedom. Hinge joints are found in the center of the leg because they do not need the same stabilization muscles as they are perpendicular to the plane of movement (Blickhan and Barth 1985). From a more global view, when all eight legs are in contact with the ground, the spider's locomotion system has 94 degrees of freedom – a daunting mathematical modelling task (Gasparetto et al. 2008).

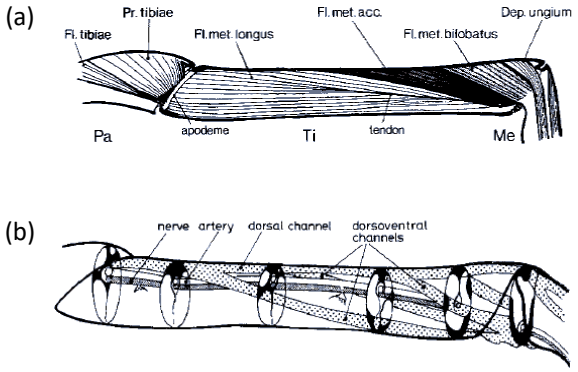

Figure 2.1 Cross section of Cupiennius salei leg
Longitudinal view of the tibia and metatarsus segments of *Cupiennius salei* showing (a) muscle organization and (b) lacunae, channels responsible for the transport of haemolymph (Blickhan and Barth 1985) .

2.1.3 Leg Extension

Like other arthropods, spiders have an open circulatory system with haemolymph vessels reaching far into the limbs. Most spider leg joints follow an antagonistic muscle design, with extensor muscles and flexors contracting and relaxing to cause extensions and flexion. The femur-patella joints and tibia-metatarsus joints do not follow this design, and lack extensors. These two joints are extended through pressurized haemolymph (Ellis. 1944; Shultz 1991). First, muscles in the prosoma contract, haemolymph is forced into lacunae (open cavities in the legs) which extend the leg joint. As haemolymph pressure increases in the leg, the dorsal joint membrane unfolds. The membrane can be compared to an accordion-like design with overlapping folds that expand when inflated. This design produces more extension torque between the distal and proximal segments compared to a bladder-like membrane design. (Nentwig 2013; Landkammer et al. 2016). The segments bordering the joint rotate on an axis located on the ventral side of the joint (Karner 1998)(Figure 2.2). The torque produced between these two segments has been shown to increase linearly with pressure.

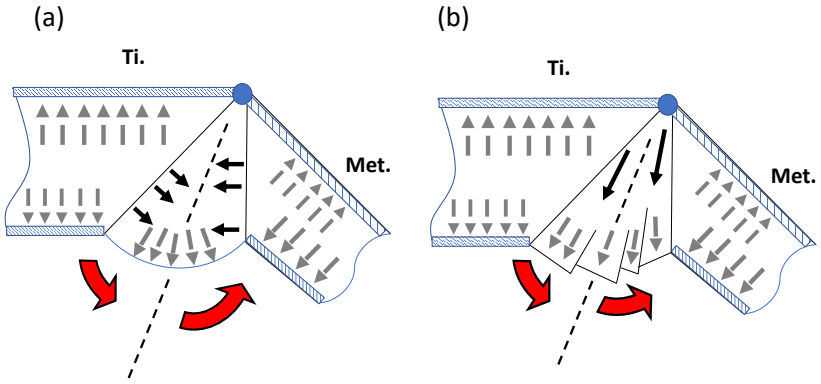

Figure 2.2: Mechanical interpretation of a spider tibia-metatarsus joint
Anticipated haemolymph pressure forces (grey arrows) and tangential forces (black arrows). Resulting torque quantities are represented by red arrows. Presented is a comparison between two interpretations of the spider joint mechanical design: (a) the membrane expands as a bladder of uniform thickness, (b) the membrane has an accordion-like structure with expanding folds.

2.1.4 Biomimetic Leg Design

The hydraulic mechanism and the biomechanical principles of the spider joint have been studied extensively and applied for biomimetic purposes (Landkammer et al. 2016). The spider leg system and methods of actuation are a source of inspiration for soft compliant robotics that are lightweight and easily reproducible. As additive manufacturing becomes cheaper and faster, pneumatics becomes preferable to rigid actuators or hydraulics (Blanes et al. 2014). Hence, the dexterity and compliant behavior of the spider leg has led researchers to emulate its characteristics in the biomedical and rehabilitation industry (De Greef et al. 2009; Belforte et al. 2014). Several designs have been developed that mimic the structure of the spider joint; some designs directly copy the mechanism, while others are an abstraction of the biological model (Landkammer et al. 2016). Menon and Lira (2006) created a segmented fluidic actuator inspired by the spider hydraulic joint that deflected under high pressure for space applications. Zetner (2013) first proposed a pneumatic design inspired by the spider joint that could be used as industrial grippers. The published design was a hollow monolithic silicone tube with coherent joints that bent up to 90 degrees under pressure (Nentwig 2013). Sprowitz's (2017) design closely resembled the bellow structure of the spider leg; it inflates using pneumatic pressure and a tendon mechanism to flex and extend a segmented plastic joint. The joint is composed of an inflatable bag enclosed in a three-piece sliding shell. The joint extends with high torque under low pressure, but the authors admitted that a simpler design would be favorable over their more complicated model. Similar to Sprowitz's design, Landkammer (2014) modeled a joint that included bellowed joint elements that extended and flexed under pressure. In his design, two connected hollow tubes encasing hyperelastic bellows, could be extended by increased pressure and flexed by a Mckibben muscle (see Chapter 2). Landkammer's design accurately employs the working principles of the spider joint. These past studies have offered conceptual biomimetic designs that embody the mechanistic principles of the spider joint, yet do not incorporate them into a complete leg design. They have investigated the joint as a stand-alone mechanism that can be used in industry. In contrast this study seeks to create a fully operating biomimetic leg as a tool for understanding spider behavior and on a larger scale, legged locomotion. An operational pneumatic leg would inform future research about spider leg actuation and the importance of the femur-patella and metatarsus-tibia

joints in leg flexion. This present study aims to offer a simple, reproducible, pneumatic design modeled on a *Dolomedes aquaticus* leg.

2.2 Materials and Methods

2.2.1 Design of Spider Leg

Sensenig and Shulz (2003) proposed that the transarticular sclerite spanning the arthrodial membrane in between leg segments could serve an elastic function. Similar to a compressed spring, the authors stated that as the joint flexed, it temporarily stored mechanical energy and could be recovered as the leg extended. That same stored mechanical energy could be recovered in elastic recoil as the leg extended (Sensenig and Shultz 2003). As mentioned in 1.1.3, a hydraulic antagonistic muscle system is responsible for the flexion and extension of the spider leg. Like past studies, I incorporated these key features into the leg design. In initial prototypes, I built and tested a hydraulic joint system, but flexion and extension were delayed and slow (Figure A.1). Consequently, a pneumatic system was chosen over a hydraulic system because it is both lighter, less complicated, and less prone to leakage. To simplify the leg further, a mechanism that mimicked the function the of antagonistic muscle in a biological spider was not included. The elimination of this design feature was unlike designs presented in past research (Landkammer et al. 2014). Instead, a flexible yet stiff joint provided the elastic recoil necessary to return the leg to its relaxed shape after extension. A second prototype featured a hybrid hydraulic – soft bladder system (Figures A.4 - A.6) but like the first hydraulic prototype, there was a lag in flexion and extension, and as an added drawback, it leaked. After the first two prototypes, a final design was settled upon: a pneumatic bladder surrounded by a rigid tubular exoskeleton and a flexible backbone.

2.2.2 Exoskeleton CAD design

CAD designs were based on Stefan Reußenzehn (2010) in vitro micro-computer tomography (micro-CT) scan of a *Dolomedes aquaticus* specimen. The micro-CT scan was converted to a 5MB file containing a 3D surface mesh model with 35,618 vertices and 37,132 faces. The 3D mesh file originally compiled on Autodesk Maya v. 2011 (Autodesk Inc., San Rafael, CA, USA) was

transferred into Auto Desk Fusion 360 v. 2.0 2018 (Autodesk Inc., San Rafael, CA, USA), a 3.D. modelling and engineering program. In Fusion 360, from the dorsal view, the right front leg of the second pair was used as a template for the leg exoskeleton design. When modelling the final armature, beginning at the trochanter segment and finishing at the tarsus, the mesh model was simplified to decrease computer lag time. The uploaded polygon mesh was reduced in the mesh workspace by a density factor of 0.253, so the femur joint alone, for example, was reduced from 1372 triangular faces to 372 faces. Afterwards, the mesh was converted into a boundary representation (BRep) model to more effectively manipulate the geometric structure. The leg was isolated from the rest of the model and a centerline drawn down the center axis of the leg from the trochanter to the tarsus. Cylinders of approximately the same length and diameter were overlaid on each segment. Each cylindrical segment was connected with a curved hinge joint. The initial prototype legs were 3D printed in polyester filament and statically tested on a hexapedal body to determine weaknesses in the leg design. Later designs had thicker trochanter-femur and femur-metatarsus joints in comparison to earlier leg prototypes which were more prone to stress from flexion forces.

In the final prototypes, joint cavities were shortened to allow for a slim fit of the pneumatic bellow. Walls were added to the ends of the joints to provide a surface for the inflated bellows to press against. The backbone for the spider leg was created separately as this needed to be more malleable and elastic compared to the other leg segments (Figure 2.3).

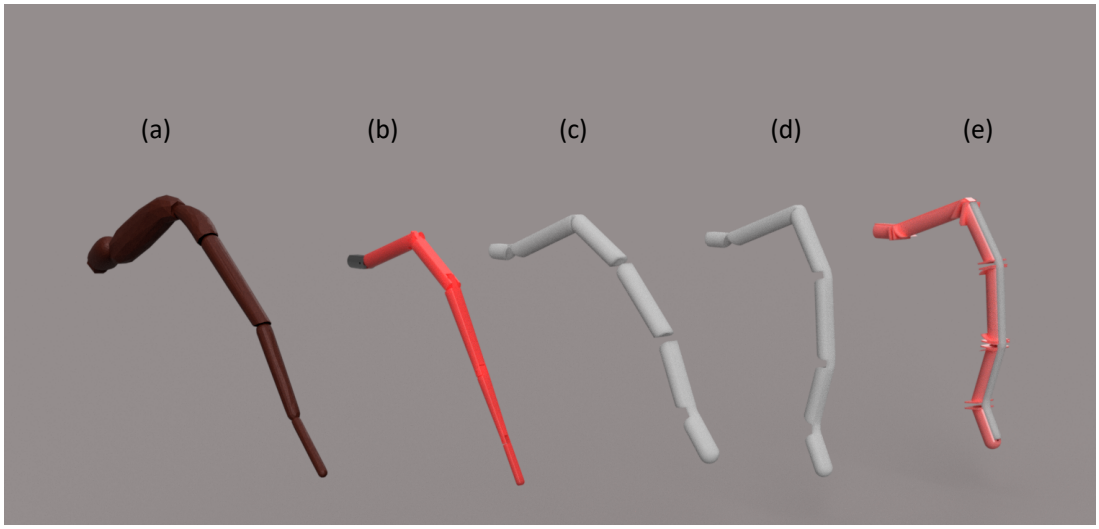

Figure 2.3 Biomimetic spider leg evolution
Fusion 360 leg design progression. (a) original 3D rendering of the 2nd leg of the Dolomedes micro-CT scan. (b) Biological model translated into a six-segment hinged joint leg. (c) monolithic compliant leg interpretation of the biological 3D rendering. (d) Angle of the femur-patella joint was steepened, and joints flattened and thickened. (e) Final leg with five ABS components and a separate ABS/PP backbone, innervated by an inflatable pneumatic membrane

2.2.3 Exoskeleton Materials and Fabrication

In order to produce versions of the spider leg quickly, they were reproduced on either a Prusa MK3 MMU2 3D printer (Prusa 3D, Prague, Czech Republic) or an Anycubic Photon-S UV Resin LCD printer (Anycubic, Shenzhen, China). Both of these printers are examples of additive manufacturing where an object is produced through layered material. The Prusa MK3 MMU2 is an example of a fused deposition modelling (FDM) printer that extrudes thermoplastic material in layers according to XYZ coordinates to produce a final product. The Prusa MK3 can potentially create high quality prints with 0.05mm layer height (Fig.A.7). The Anycubic Photon-S is a stereolithography (SLA) printer. Similar to the FDM printer, the SLA printer projects a UV layer on the bottom of a photosensitive resin bath and causes resin, composed of chemical monomers, to bind into polymers creating a solidified layer. The added advantage of SLA printers over FDM printers is they can produce higher-quality objects ranging in layer height from 0.01 mm to 0.0025 mm.

Leg prototypes produced on the Prusa MK3 were printed in Acrylonitrile butadiene styrene (ABS), Thermoplastic polyurethane (TPU), Polylactic acid (PLA), Polyester, and Polypropylene (PP). For the final prototype, the leg segments were printed in ABS as this was the most durable material of the listed materials above. PP was the most suitable material for the leg backbone as it was elastic, light, but most importantly the joints would not break as the leg extended.

Leg prototypes produced on the Anycubic photonS were printed with Monocure 3D Rapid Resin (red, blue, green, gunmetal grey) and Monocure 3D Flex 100 (Monocure 3D, NSW, Australia). Flex 100 can be added to normal resin in a ratio of 10:90 to 30:70 with good results depending on desired final object flexibility.

During initial prototyping, legs were not produced as monolithic pieces but as segmented joints connected with different materials. These joint prototypes were connected with casted latex, casted silicone, TPU and piano wire (Figure A.1).

Designs produced on Fusion 360 were saved as a stereolithography (STL) files and uploaded into Prusa Slicer V. 2.10 (Prusa 3D, Prague, Czech Republic), a preparatory 3D printing software. Once in the slicer software, finer details regarding 3D printer presets were manipulated and the final object converted into G-code, a numerical control programming language.

2.2.4 Pneumatic bladder CAD design

For the design of the inner membrane of the spider leg, measurements were taken from the Fusion 360 exoskeleton drawing to determine the size and shape of the final silicone mold. The radii of the six leg segments were compiled to create a hollow membrane design with protruding bellows at exposed joint intervals. A two-part mold was designed on fusion 360 and printed on the Prusa MK3 with ABS, printed at a 0.1mm extrusion radius to produce a more detailed print. Silicone was subsequently poured into the first half of the mold and secured with the second half. In the first design, after casting fabrication, the bellows of the pneumatic bladder were very shallow and flexed minimally. Consequently, in subsequent designs, the bellowed segments were increased radially and the walls thinned. Early bellowed segments also tore in the mold-removal process so

the mold walls were rounded. The resulting final mold was separated into two halves - a base and a lid with the dimpled impression of the air chamber and bellows.

2.2.5 Pneumatic bladder Fabrication

For each iteration of the spider leg bladder, three different materials were tested: Smooth-Sil™ 940 (Smooth-on, PA, USA), Eco Flex™ 00-30 (Smooth-on, PA, USA) and liquid latex (EnvironMolds, NJ, USA). First, liquid latex was quickly ruled out as a material choice as the latex needs to be exposed to air to cure. Secondly, Cured Eco Flex™ 00-30 produces a tacky final product and is not suitable for small moulds with fine detailed features. Finally, Smooth-Sil™ 940 (Smooth-on, PA, USA) was a preferable choice of casting material as it is robust, non-tacky, and captures high relief details. Smooth-Sil™ 940 is a non-toxic two-part mix with a colored hardening agent and a master mix. The hardening agent is mixed into the master mix in a 1:10 ratio and mixed for approximately 3 minutes. The final silicone mix takes approximately 30 minutes to condense, and 24 hours to completely cure. During mixing, air bubbles are introduced which can create a leaky final bladder. To decrease the chance of introduced air bubbles, 7 grams of the final mix were poured in the first half of the mold and placed in a 3-gallon vacuum chamber (Happy1 Watering Store, China) to degas for 15 minutes at 0.9 Bar. The final degassed silicone mixture was removed from the vacuum chamber and the 2nd half of the mold placed gently in the 1st half of the mold. The entire mold complex was fixed to a workbench with parallel clamps to assure the two halves of the mold would not shift during curing.

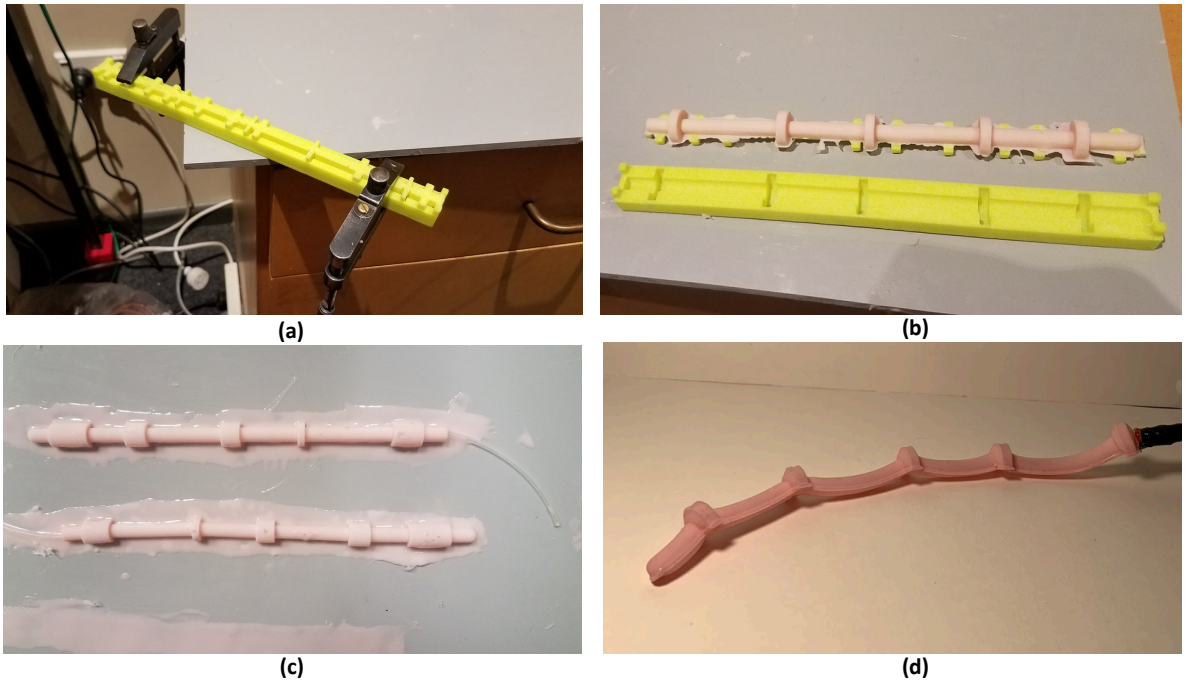

Figure 2.4 Pneumatic bladder fabrication
Progression of Pneumatic bladder fabrication. (a) Silicone is poured into the first half of the mold, degassed, and sealed with the second half of the mold. The entire mold structure is tightened with parallel clamps. (b) After 24 hours the two mold halves are separated and excess silicone trimmed from the first half of the silicone bladder. (c) A layer of silicone is lathered onto a PVC sheet and the cured half of the silicone bladder placed on the uncured layer. The two layers are bonded with uncured silicone and a piece of polyethylene tubing is inserted at an opening of one end of the bladder. (d) The base layer is trimmed, and the bladder inflated to check for air leaks.

The mold cured for 24 hours and was removed using a scalpel and putty knife. The edges of the bladder were trimmed and analyzed for micro-bubbles. 5 grams of Smooth Sil mix was applied to a grey ABS board using a putty knife, and the cured top bladder nestled into the wet silicone. A polyethylene tube (OD: 3mm, ID: 2mm) was inserted into the rear of the silicone bladder and covered with 1 gram of silicone mix. After a further 24 hours of curing, the excess foot of the bladder was trimmed, and the bladder inflated with a 30ml syringe to test for air leaks (Figure 2.4).

2.2.6 Final Leg Fabrication

Fusion 360 allows one to create an object with specific dimensions, but these dimensions are arbitrary and inaccurate when converted to another program. During the conversion process from an STL file to G-code, the model can change in scale. The backbone, the bladder, and segments were all based on the same CAD measurements but printed off in 1% scaled increments with the bladder printed off at 49% of the original drawing, the segments printed at 50%, and the backbone printed at 51%. Because of the size variation during conversion, the bladder of the final structure needed to be slightly smaller in scale compared to leg segments and backbone so that it would fit securely in the segment recesses. The exoskeleton segments also needed to be shrunk slightly from their original design size so they would fit snugly onto the leg backbone. This scaling method produced the best fit pneumatic leg. Once the bladder and segments were fitted in place, the segments were individually glued on to the PP backbone using Smooth-On (Sil-Poxy™) and Loctite Super glue (Loctite, Düsseldorf, Germany)(Figure 2.5).

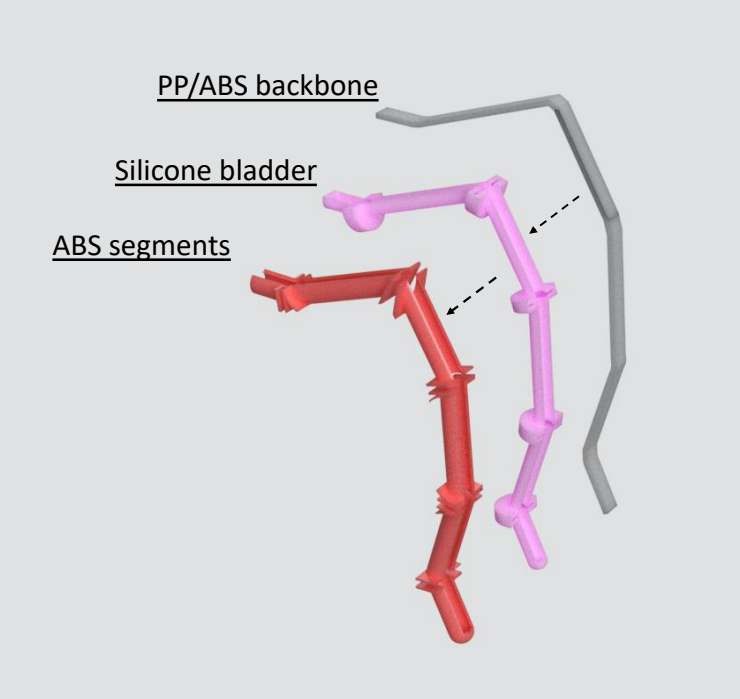

Figure 2.5 Final Leg Fabrication
Illustration of pneumatic leg components. The silicone bladder sits within the ABS joint segments and is sealed with an ABS/PP backbone

2.3 Analysis

2.3.1 Parametric Pneumatic bellow design

A finite element analysis (FEA) simulation was conducted on the final design of a five-bellowed pneumatic bladder. The FEA simulation was run on a model designed within Fusion 360. The dimensions for the bladder are as follows: 462 mm chamber length, 2 mm uniform wall thickness, 14 mm diameter for major bladder neck, and 31 mm bellow diameter. These parameters were optimized over several pneumatic bladder designs. The simulation in Figure 2.6 predicts the motion-force profile and the deformation of bellows under high pressure. The pressure profiles of these specific simulations varied between 100 kpa and 500 kpa. PDMS material was substituted for Smooth-Sil™ 940 in FEA simulations, as the latter was not available material choice but PDMS has similar density and Young's Modulus values (Table 2.1).

Table 2.1: PDMS material properties

PDMS (**Polydimethylsiloxane)**	
Density	1.25E-06 kg/mm^3
Young's Modulus	0.0001 GPa
Poisson Ratio	0.49
Yield strength	10.34 MPa
Ultimate tensile strength	6.5MPa
Thermal Conductivity	2.275E-04 W/(mm C)
Thermal expansion coefficient	8.1E-06 / C
Specific Heat	1880 J/Kg C

FEA analysis of a static stress test of the inner membrane was run in Fusion 360 with an inner pressure of 500 kpa. The face at the posterior end of the bladder was used as a grounded point and the face running on the dorsal side of the bladder assigned as a frictionless surface for the actuator to move under pressure. An overall linear expansion of the bladder was observed when inflated to 500 kpa. Most of the stress and radial deformation is localized in the five bellows. The bellows ballooning leads to the twisting motion observed in Figure 1.2.4a. There is minimal radial

expansion observed in the bellows with overall stress and deformation localized to these five areas. A greater surface area lends to a larger ballooning effect in the bellows. The FEA simulation in Figure 2.6 depicts the safety factor layout of an object under a load but is also a proxy for von Mises stress projection, a colored graphic depicting the color contours of yield stress values.

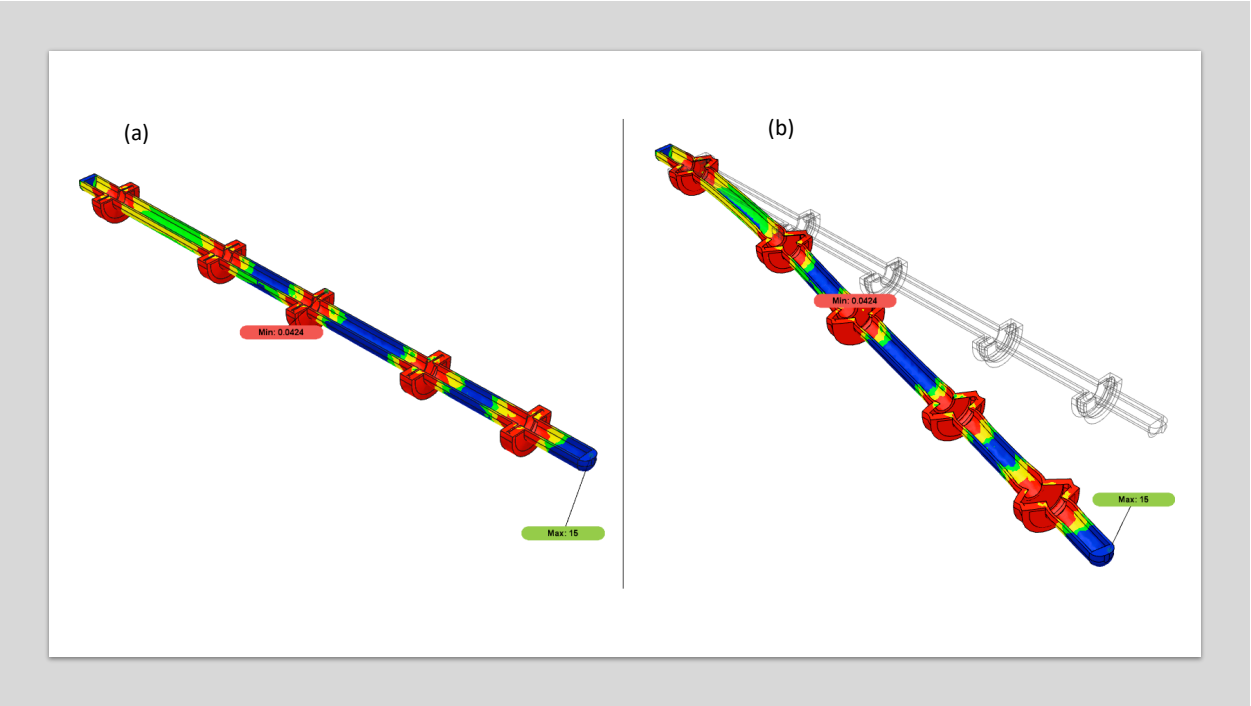

Figure 2.6: FEA simulation of pneumatic bladder
FEA simulation of a semicircular pneumatic bladder with a single tube and 5 bellows (total length = 231 mm) actuated in one degree of freedom. Colors encode safety factor, a direct proxy of stress values. Areas highlighted in blue show an area of high safety factor/low stress under pressure, whereas areas highlighted in red demark an area of high safety factor/ high stress under pressure. (a) the pneumatic bladder at 100 kpa (resting state) and (b) 500 kpa (max flexion) with a minimum safety factor of 0.042 and max stress of approximately 175Mpa.

2.3.2 Influence of Backbone material on flexion

Two separate pneumatic spider legs were created, one with an ABS backbone and the other with a PP backbone. It was expected that the leg with the ABS backbone would flex less under a set pressure compared to the PP backbone, because the compliant PP backbone deforms more under a consistent pressure compared to the ABS backbone (Figure 2.7). Legs were mounted on a fixed box, with the tarsus making contact with the ground. What is not seen in figure 1.2.4 is the polyethylene tube (OD: 3mm, ID: 2mm) attached to a 30 ml, undepressed syringe. Pressure was

measured using a differential pressure sensor (DPS)(MPX5010DP NXP, Jaycar, Dunedin, NZ). Both legs were inflated to 180kpa, and pictures taken of the maximum flexion positions. Still shots were taken of the fully inflated legs and imported into ImageJ (Rasband, W.S., ImageJ, U. S. National Institutes of Health, Bethesda, Maryland, USA). The change in angle from the leg's initial position to its flexion point was measured with the angle tool in the ImageJ. When both legs were inflated, greatest deflection was observed in the femur-patella joints and tibia-metatarsus joints, irrespective of the joint material. For the ABS leg the femur-patella flexed 10° and the tibia-metatarsus joint flexed by 11.6°. For the PP leg the femur-patella joint flexed 19.9° and the tibia-metatarsus joint flexed by 13.6°. Overall, the PP leg lifted 78.5 mm off the ground compared to the ABS leg's 46 mm of travel (Figure 2.7).

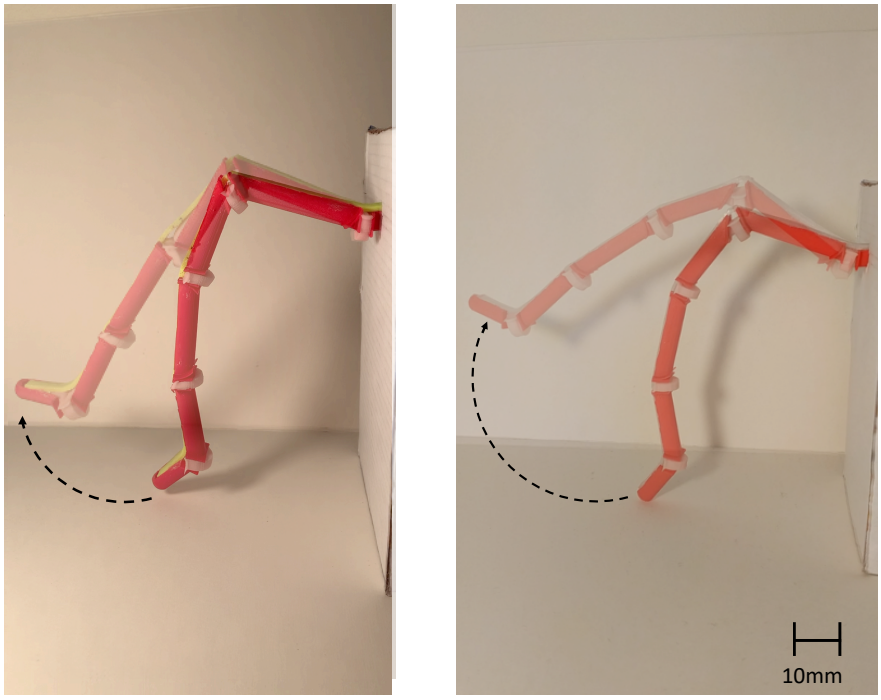

(a) **(b)**

Figure 2.7: Flexion comparison of pneumatic legs
Maximum flexion comparison between pneumatic spider legs with either (a) ABS and (b) PP backbones. Semi-transparent shots of the fully inflated spider legs are overlaid on top of clips of the legs in their initial resting positions.

2.4 Conclusion

This study represents a novel method of using additive manufacturing to rapidly produce prototypes that accurately capture a biological organism's body design. Early in the design process, attention was focused on making the leg compliant rather than mechanical to capture a spider's innate nimble behavior. To test compliant legs, joint design could be modified quickly and tested using an FDM printer, and an SLA printer. Prototype legs could be manufactured in PLA, TPU, Carbon-PLA, ABS, Polyester, and PP to determine an ideal ratio between joint flexibility and stiffness.

Concurrently, pneumatic bladder prototypes could be fabricated and tested from molds produced on the FDM printer. The SLA printer was used, but the photosensitive resin reacted poorly with the silicone, leading to variable curing rates. Even though the FDM printer does not produce the same quality of molds as an SLA printer, the molds produced were adequate and comparable in quality to the SLA molds. From these molds, silicone (SmoothSil and ecoflex) and latex bladders were produced and tested to determine which bellow material would present the most ideal inflation qualities. Some of the qualities included bellow tensile strength durability when inflated, and ease of manufacturing. Silicone was chosen for its ability to be easily manufactured and the lack of final prototype tackiness.

In the final design the bladder, stiff leg segments, and PP backbone were all joined together to complete the final leg. Overall, it performed better than expected considering the high failure rate of past prototype bladders. The PP backbone leg performed markedly better compared to the ABS backbone. The rigidity of the ABS backbone countered the inflating silicone bladders leading to minimal flexion. Opting for a PP versus an ABS backbone made the leg more pliable and flexible under pressure. The optimization and enhanced performance are mostly qualitative indices that are visually validated. The only concrete quantitative validation of the increased performance of the PP versus ABS design, was the measurement of angle deflection when inflated (Figure 2.7).

2.4.1 FEA analysis

The FEA simulation presented in Figure 2.6 is an accurate representation of the behavior of the pneumatic bladder under pressure. The actuation characteristics are similar to what was observed in experimental trials with a fabricated silicone bladder. However, the pressure loads of 500 kpa in an actual lab setting would have inevitably caused the bladder, especially around the bellows, to rupture and fail. This disparity between the real and simulated pressures applied to the bladders could be due to the FEA software. The simulation provided in Fusion 360 may be suited for basic static stress tests on large robust objects made of durable material, but not for hyperelastic Mooney-Rivlin (i.e. silicone) material tests. It is not known if any past simulations using hyperelastic materials have been performed in the simulation platform of Fusion 360. Elsayed et al. (2014) presented an optimized design of a three-chamber silicone actuator using three silicone grades: Ecoflex 0030, Ecoflex 0050 and Dragonskin 0030, silicone types with similar shore-hardness values to SmoothSil 940. The cylindrical actuator was 25mm in diameter, 65mm in length, and had a 1.5mm thick wall. In FEA simulations their actuator flexed at 90° under 32kpa in one degree of freedom. Their applied pressure stands in stark contrast to the simulated pressures in this study required to flex the proposed pneumatic bladder. Simulations of hyper elastic materials similar to the ones Elsayed et al. conducted (2014), should be conducted in Ansys, a specific engineering software.

2.4.2 Prototype leg flexion versus biological leg flexion

Overall there was more leg movement observed in the biological spider leg versus the prototype presented in 2.3 (Reußenzehn 2010; Parry and Brown 1959). Most of the leg articulation in this review focuses on the femur-patella and tibia-metatarsus joints which can be viewed as purely hydraulic hinge joints operating with one DOF. In a study conducted by Parry and Brown (1959), common house spider (*Tegeneria atrica*) legs were isolated from the cephalothorax and injected with fluid to determine joint angle change with increased pressure. As the pressure increased from approximately 4 kpa to 10 kpa the femur-patella joint angle increased by 80 degrees. In the tibia metatarsus joint, as the internal pressure increased approximately from 4 to 8 kpa, the joint angle

increased by 120 degrees (Parry and Brown 1959). In the Reußenzehn (2010) study, individual *Dolomedes* legs were injected with fluid to determine the range of movement for individual joints. As hydrostatic pressure was increased to 6.8kpa, femur-patella joint angles increased by approximately 100 degrees and the tibia metatarsus joints by 70 degrees. The change in flexion angle of the presented prototype femur-patella and tibia-metatarsus joints presented in this study, differ substantially from past isolated joint angle measurements of two different spider species. Specified in 2.3.2, femur-patella joints and tibia-metatarsus joints only shifted by 19.9 and 13.6 degrees in the PP leg. The minimal change in joint angle shift of the fabricated leg versus the biological leg may point to the need for further alterations of the prototype joint (elaborated on in 2.4.3). The silicone used for the bladder may still be too stiff compared to the biological spider membrane, or the isotropic silicone membrane design may not allow for a larger range of movement when inflated.

2.4.3 Future design modifications

In the initial stages of the bladder design, a monolithic tube with 5 rounded bellows seemed the most suitable approach to a working prototype. The bellows are mechanically isotropic and simply shaped making them easy to caste in silicone. Blickhan and Barth (1985) found that the spider articular membrane is folded like an accordion (Figure 2.2) and displays minimal axial tension when inflated unlike a uniformly thick isotropic bellow design. Landkammer et al. (2015) and Nentwig (2013) both approached the design of a biomimetic spider leg considering Blickhan and Barth's (1985) findings. While the bellowed membrane presented in this paper did not follow an accordion membrane design, there was suitable inflation in the membrane to cause noticeable flexion in the leg. Bearing that in mind, future membrane designs should include a folded accordion-like membrane as this would reduce torques generated by inflation of the bellow and possibly lead to greater extension.

In the current design, the legs consist of six cylindrical tubes of equal diameters but varying lengths. The leg segments follow the length and angle orientations outlined in Reußenzehn's (2010) thesis. However, in future prototypes, the leg segments from the coxa to the tarsus should be scaled down radially according to the specifications of the Reußenzehn's (2010) micro-CT scan

of the *Dolomedes aquaticus* specimen. Reduced radial distal leg segments would lead to a proportional decrease in weight. The swing phase is a key part of the spider leg gait cycle where the leg shifts aerially from a posterior to anterior position. A decreased distal swing weight, from radially reduced segments, would lead to less rotational inertia and increased energy conservation of a hypothetical robot.

The presented spider leg was created as a monolithic model with flattened, thickened joints to operate in one degree of freedom and decrease lateral movement. A PP backbone allows for increased leg compliance versus an ABS backbone, but the PP backbone has an increased occurrence of lateral and rotational deflection in the joints compared to the stiffer ABS backbone. A possible solution for these aberrant deflections would be to run guide wires down the sides of the leg segments to provide lateral support and dampen external perturbations.

3 Novel Design Pneumatic Mckibben Muscles

3.1 Introduction

3.1.1 Pneumatic Muscle background

Mckibben muscles are pneumatic actuators that exhibit behavior similar to biological muscle and are used in robotics and industry (Klute et al. 1999; Chou and Hannaford 1996). In modern industry it is advantageous to have robots driven by pneumatic actuators because of their innate compliance. To operate in uncontrolled environments or engage with fragile objects, actuators should exhibit dampened, spring-like behavior.

The dynamic and static properties of muscle include their innate ability to store energy when stretched. The viscoelastic properties of muscle and tendon allow them to act like springs, storing energy. This allows for an organism to reduce metabolic energy expenditure during locomotion. In walking and gripping robots, mechanisms that replicate the elastic behavior of biological muscle are included in design. Pneumatic air muscles, pressurized bladders surrounded by a woven sheath, mimic the compliant nature of biological muscles when contracting and extending. Pneumatic actuated muscles (PAM's), are a lightweight alternative to conventional motors by using pressurized low-density gaseous fluids. The compressibility of gaseous fluids, such as air, lend to compliant, soft systems which exhibit high power-to-weight ratios. In contrast, these characteristics differ from hydraulic and mechanical systems which have rigid behavior. Hydraulic fluid is relatively incompressible compared to pneumatics, while mechanical systems use a series of rigid linkages or components to generate power.

Within the larger family of PAMs are Mckibben muscles (MKM). Joseph L Mckibben is credited with popularizing the artificial muscle in the 1960's within the orthotics industry (Nickel et al. 1963). The MKM design is simple: An internal expanding membrane (i.e. rubber, silicone, other polymers) is surrounded by a double helical weave mesh (Figure 3.1). When inflated, these actuators axially contract followed by radial expansion creating a 'bulging' appearance (Figure 3.2). The axial contraction generates a pulling force on an attached load. At the same time, the

MKM acts as an inverse bellow, differentiated from pneumatic bellows which extend axially upon inflation (Daerden and Lefeber 2002).

The MKM's compressibility results in increased safety in man-to-machine contact and because of this feature have been adopted in robotics for biomechanical applications, prosthetic devices, and industrial applications (Gordon et al. 2006; Villegas et al. 2012; Van Damme et al. 2005).

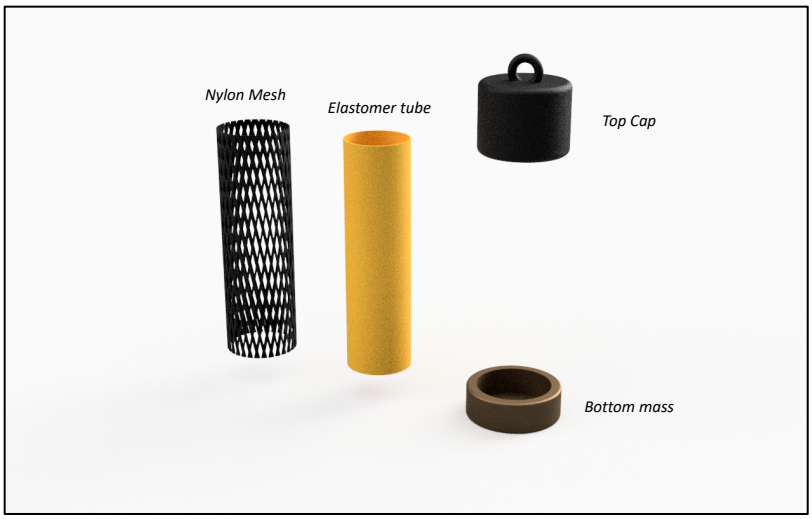

Figure 3.1: Traditional MKM Design
Elastomer tube within an expanding mesh. Both components are fitted with a top and bottom cap.

3.1.2 Comparison between skeletal muscle and artificial muscle

Actuators, components responsible for moving a mechanism, should be robust and energy efficient. Biological muscle-tendon systems possess these desirable properties and have the added benefit of being lightweight, elastic, and impact dampening. Simplified models of muscle have been produced to predict the relationship between force, length, and velocity of muscle behavior (Klute et al. 2002). For example, simple models such as the Hill-model include a contractile element, a series elastic element, and a parallel elastic element (Dzahir and Yamamoto 2019). These simple models help to accurately predict how pneumatic muscle behave compared to their biological counterparts. Models can inform and predict the contractile and passive and spring-like properties of an MKM depending on inner-pressure and stiffness. MKMs behave and emulate their

biological counterparts by having similar contractile and passive spring-like properties. Their elasticity is dictated by the proportional relationship between stiffness and inner pressure.

The artificial muscle is designed to emulate skeletal muscle with the force-length relationship between the two muscle types being similar (Klute et al. 1999). Chou & Hannahford (1996) demonstrated a static force-length mathematical model of MKM behavior and compared it to the biological muscle Hill-model (Surentu et al. 2007), demonstrating that measured experimental behavior follows a similar linear trajectory compared to the predicted model results. These studies demonstrate that biological muscles and artificial muscles share similar dampening and spring-like qualities.

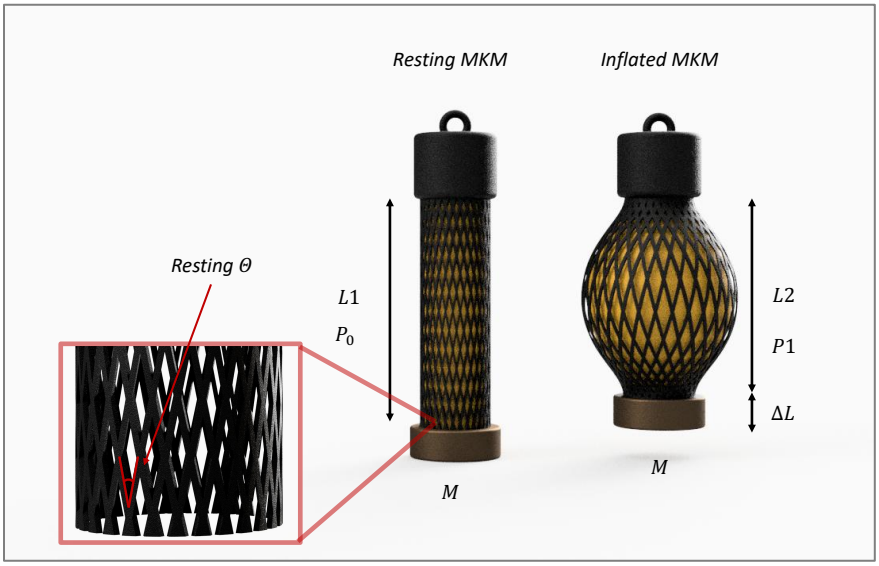

Figure 3.2: MKM behavior
MKM behavior comparison at rest and when inflated. Resting sheath angle is denoted by (θ). Resting length (L1) and resting pressure (P_0) is compared to final inflated length (L2) and inflated pressure (P1), with (ΔL) presented in the inflated MKM diagram. An attached mass (M) is used in loaded isotonic tests.

3.1.3 Non-linear behavior and Friction

MKMs exhibit non-linear behavior that stems from the viscoelastic properties of the inner tube, the hysteresis of the inner tube under pressurized conditions, and the compressibility of air; all of these factors make it difficult to predict MKM contraction behavior (Tondu and Lopez 2000; Meller et al. 2014). Another drawback to MKM design is the coulomb friction, or dry friction, that

occurs as the mesh shell slides over an inflating inner bladder. This friction is difficult to predict, but it is suggested to add 2.5 newtons to the overall friction value when testing pneumatic actuators (Chou and Hannaford 1996). To address unnecessary sliding friction and control non-linear behavior, this study proposes embedding the mesh sheath within a castable elastomer shell. Past studies have embedded Kevlar threads and flexible plastic plates to cause linear contraction of the actuators. Multimodal sensors have also been embedded to determine contraction displacement (Park and Wood 2013; Wirekoh et al. 2019). The present study addresses the uninvestigated concept of a monolithic MKM where the sheath and elastomer are casted together, to increase repeatability and improve automation of production. For this study, silicone-casted MKMs were compared to latex-casted MKMs to determine which material best suited a monolithic MKM design.

3.2 Materials and Methods

3.2.1 Design of Mckibben Muscles

MKMs are comprised of two main entities: the double helical weaving sheath and an inner elastic bladder. The bladder is covered by the sheath and, as it is inflated, the radial swelling is constricted by the sheath causing the system to contract axially. However, this is not a frictionless system as the sheath rubs against the bladder as it is inflated. This has proved to be inefficient and hence, alternative designs should be considered to reduce this energy loss. Alternatively, this study proposes that the sheath and rubber bladder be cast as a monolithic unit, to negate sliding friction.

3.2.2 Materials and Fabrication

Expanding plastic braiding was ordered from AliExpress (AliExpress, Alibaba Group, China). First, the 8mm diameter braiding was cut into 100mm segments. Each segment was stretched to reduce the inner diameter and ensure maximum contraction upon inflation. Second, the elongated braiding was stretched tightly over steel mandrels (diameter: 3mm, length: 150mm)(Figure 3.3).

Before the casting process, an in-house release agent was created and brushed on each mandrel so casted tubes would not adhere and tear when they were removed. The release agent is a solution of water, liquid detergent, chalk, and talcum powder (1:1:1 mix ratio) which was mixed and applied to the outside of the mandrels. This mixture follows a similar coagulant solution used in latex balloon production as the liquid detergent allows the latex to spread in an even film, the talcum powder is a release agent, and the chalk acts as coagulant (Rottner, 2019)

Two different approaches were taken for casting the prototype MKMs. The first approach used a vacuum casting method, and the second approach involved a "brush-on" method. In the first approach, steel mandrels were place in a 3D printed mold (ABS plastic), uncured silicone forced into a recess resulting in an elastomer tube (length: 50mm, inner wall:1mm). After curing, the elongated sheath was placed over the casted tube and put into a second 3D printed mold with a wider cavity, such that when vacuum-casted, produced the final monolithic MKM (length: 50mm , inner wall: 3mm)(Figure 3.4).

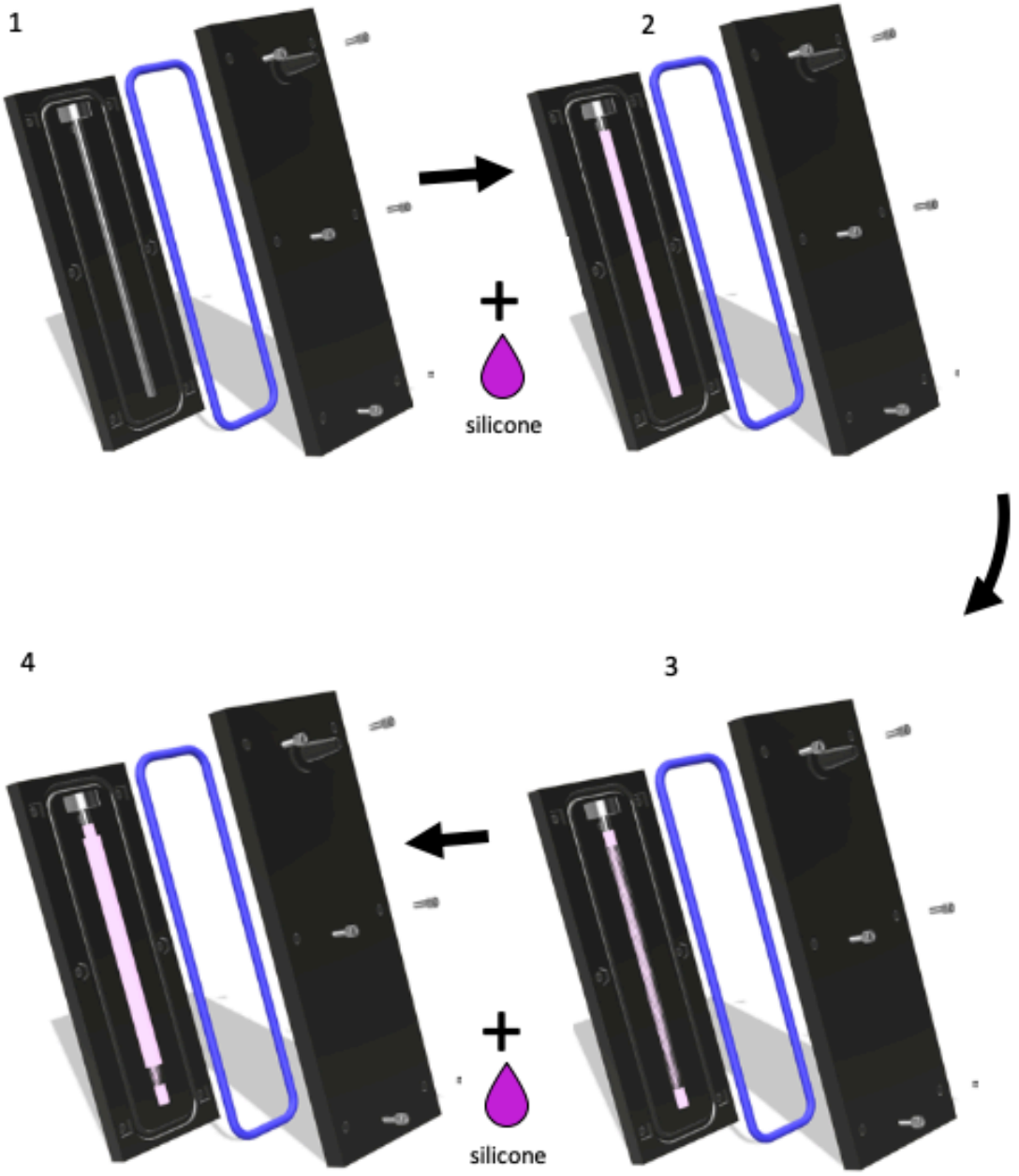

Figure 3.3: Visualization of Vacuum Silicone MKM Fabrication
(1) 3 mm steel mandril is placed in the alpha section of mold (1mm gap between mold and mandril. A Blue rubber O-ring fits into the alpha mold recess. Beta mold is bolted into the alpha mold with six hexagonal nuts. Silicone is forced into the mold through a TPU valve. (2) The mandril and silicone tube are released from the first two-part mold after curing for 24 hours.(3) 2mm double-helical plastic weave is fitted over the first layer of silicone tube. The mandril, silicone tube, and mesh weave are placed into a second two-part mold with a 2mm gap between the mesh and alpha mold. The beta mold is fixed to the beta mold with screws and pressurized silicone is forced into the mold. (4) The full silicone MKM is released from the mold after curing for 24 hours and separated from the mandril. The ends of the MKM are trimmed for testing.

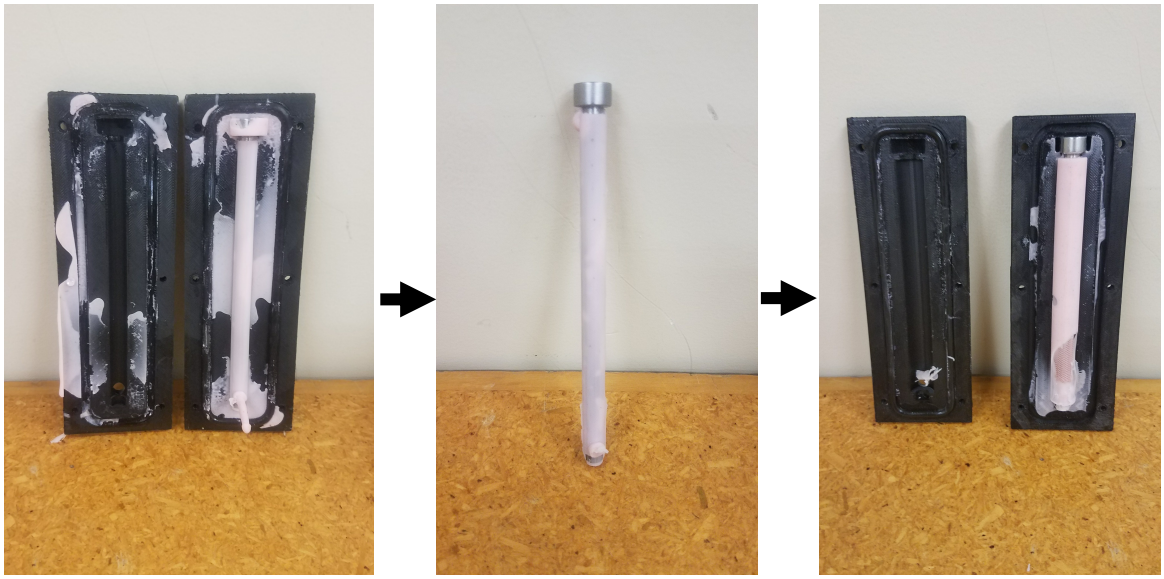

(a) (b) (c)

Figure 3.4: Silicone MKM casting process
(a) Silicone mandril post-silicone injection is release from its mold. (b) The first silicone layer is trimmed before being place in the second mold. (c)Fully cured silicone MKM is released from the second mold. Air pocket revealing the plastic mesh are trimmed from the final MKM.

In the second approach, one layer of Silicone (Smooth-Sil™ 940) or Latex (Barnes Brush latex) was painted on the steel mandrels and knitting needles (length 50mm, diameter 3mm), and dried inverted. Both mediums were stirred and strained, to maintain a uniform thickness for each bushed-on layer. Once each silicone or latex layer had cured (Smooth-Sil™ 940 - 4 hours, Barnes brushed latex – 2 hours), a second layer of the same medium was painted onto the surface of the needle or steel armature and allowed to cure again.

For the third and final layer, the elongated plastic sleeve was placed and stretched over the first two layers, and a third layer painted over the sheath and inner two-layer walls. In the initial prototype development MKM layer fabrication design was compared: a one-layer inner wall plus a sheath followed by two brushed on layers was compared to MKMs with a two-layer inner wall, sheath, and one-layer outer wall (Figure 3.5). When comparing both methods, a one-layer inner wall produced inferior MKMs that were prone to tear or leak when inflated. The latter method of MKM fabrication style (1-layer inner wall + sheath + 2 - outer layers) left the inner layer more

susceptible to tearing and separation from the outer two walls due the plastic sheath's contraction (Figure 3.5).

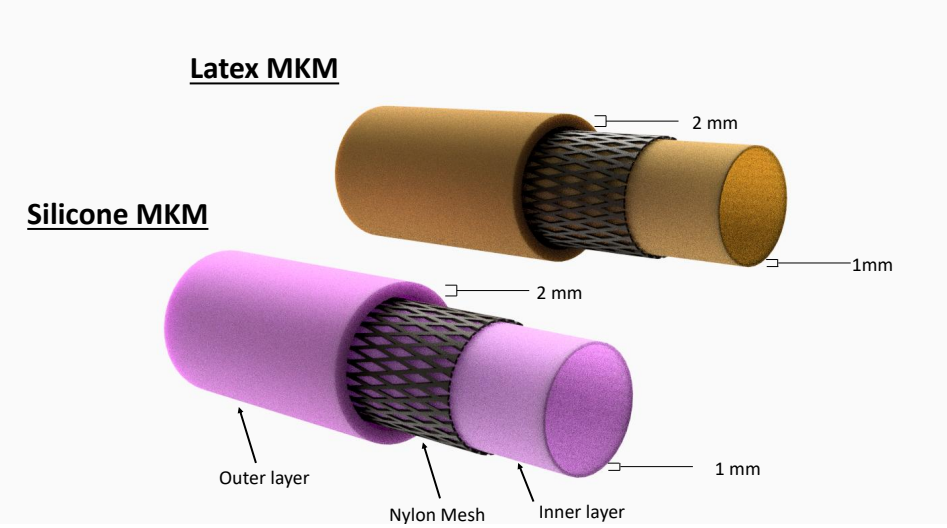

Figure 3.5: Illustration of monolithic MKM
Prototype monolithic MKM design fabricated in Silicone (Smooth-SilTM 940) and Latex. An inner layer (1mm) is sheathed in a plastic mesh, and an outer (2mm) layer.

3.2.3 Design and setup of measurement apparatus

To determine the characteristics of the prototype Latex MKMs, I designed a pressurized closed system where the MKM could be inflated. Changes in the amount of volume of air in the system, length of the MKM under pressure, and pressure in the system were measured.

A Differential Pressure Sensor (DPS) (MPX5010DP NXP, Jaycar, Dunedin, NZ) was attached to polyethylene tubing (OD 5.8, ID 3.8) which was funneled to one end of the tested MKMs. The other end of the MKM was shunted off by a one-way 3D printed valve. Attached to the valve was a suspended 60ml sample container used to hold weights.

Beneath the lab container, a piece of cardboard (34x80mm) served as an enlarged reflective surface for the Time-of-flight sensor (ToF). Perched on a stool, roughly 100mm from the bottom of the container, an adafruit time-of-flight laser-ranging module (ToF) (VL530X, adafruit, New York City) recorded the change in length of the McKibben muscle as it was inflated. A 30ml syringe

(BD syringe Slip Eccentrip Tip, NJ, USA) was used to pressurize the system. Regardless of whether the ToF was shifted, total displacement of the muscle under contraction was normalized by subtracting the length of the muscle before and after being pressurized. Data from both the ToF and DPS were relayed to an Arduino Mega 2560 REV3 and read onto a serial monitor at a 115200 baud rate. Where joints or valves were connected to sensors, prototype McKibben muscles, or to the syringe, connections were tightened and reinforced with zip ties (100x2.5mm, KSS, Taiwan).

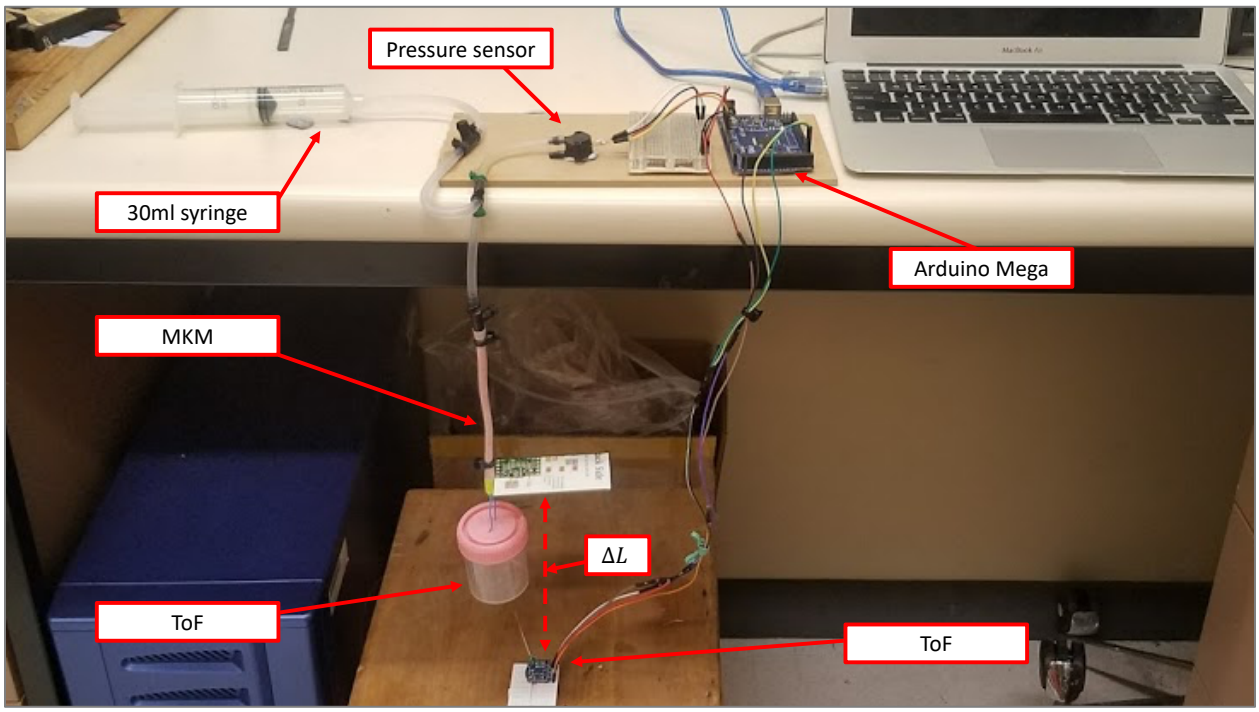

Figure 3.6: Design and apparatus setup for MKM prototypes
Design and apparatus setup for measurement of contraction, displacement, and pressure change in test MKM prototypes. Increase in pressure in the closed system from ambient room pressure (103.6 kpa) is registered by the pressure sensor. An increase in pressure leads to the MKM contraction, and a change in length denoted by the dotted line (ΔL). MKM length change is recorded by the Time of flight sensor (ToF).

3.2.4 Data Collection

Five silicone muscles were measured and compared against four latex muscles, created using the brush-on method outlined in the fabrication process above. Each muscle, irrespective of the media used, was individually attached to the specimen bottle on one side and on the other side, a piece of polyethylene tubing (OD 5.8, ID 3.8) leading to the pressure sensor and syringe assembly. To minimize leaking air, both connections on either side of the tested MKM were tightened with zip

ties. Each muscle's concentric contractions were measured with no weight, one gram, five grams, and ten grams of weight.

For each weight, five contraction trials were recorded. Before running each test, the pressure sensor was normalized to one atmosphere, or 101.325 kpa. Next, the syringe's plunger was drawn back to its peak volume of 30ml and the relaxed length of the MKM was r secorded before the start of each trial.

The serial monitor was initialized for data recording and base data recorded for 5 seconds.
The plunger was fully depressed to 0 ml, and relaxed, so the plunger returned to its initial position at a 'natural' speed. The final resting position of the plunger was recorded to calculate work efficiency – and a possible indication of hysteresis or leaking air. Serial data collection was stopped and copied into a text edit V.1.15 (Apple Inc., 2019, Cupertino, CA) file first and later, in an excel document for data processing. After 20 trials had been recorded, five trials per weight category and muscles were changed (Figure 3.6).

3.3 Data analysis

3.3.1 Normalizing time against pressure-displacement measurements

Linear regression was carried out in Microsoft excel V.16.35 (Microsoft, 2020) to find a correlation between duration of time, pressure, and displacement of the MKM muscles during each experimental measurement. Each pressure-distance measurement was recorded at 0.2 second increments. All pressure data was normalized by subtracting 1 atm (101.325 kpa) to show the overall change in pressure with each time increment.

3.3.2 Fitted models for Contraction-Force relationships

In order to derive the contraction force also known as the tension force (F_t) of both fabricated silicone and latex muscles, a theoretical equation based on energy conservation was applied derived by (Chou and Hannaford 1996). The following equation considers the diameter of the MKM muscle at rest (D_0), the current pressure (P), and the weave angle of the MKM at rest (θ). Six separate weave angle measurements were recorded from two latex MKM muscles and two silicone muscles. Both sets of six measurements were averaged to produce an average weave angle of 64.14° for resting latex muscles, and 52.28° for silicone muscles.

$$F_t = (\frac{\pi D_0^2 P}{4})[3cos^2\theta - 1] \quad (1)$$

To calculate the pulling force (F_p), or axial force of the MKM muscle, irrespective of material composition, a simple force related to area equation was applied.

$$F_p = PA \text{ or } F_p = P/\pi r^2 \quad (2)$$

In this instance, (r) relates to the initial resting inner radius (3mm) of the MKM muscle, and the total area (A) represented by the area of a circle πr^2. (P) represents the pressure and contraction at each time increment.

3.4 Results

3.4.1 Effect of Pressure on Contraction in Latex and Silicone MKMs

The relationship between pressure and contraction in both silicone and latex MKM muscles was non-linear, yet both muscles exhibited similar behavior profiles. Generally, as internal pressure increased there was a corresponding increase in contraction. Linear regression revealed a significant relationship between pressure and contraction in both Latex and Silicone MKMs. Overall, there was an average displacement of 13.23mm $\pm$ SE 0.586 at a pressure of 204.17kpa

$\pm SE$ 1.967 in the Silicone MKM. In the Latex MKM there was an average displacement 10.03mm $\pm$ SE 0.453 at a pressure 230.259kpa $\pm SE$ 2.33. Qualitatively, a sharp increase in contraction in relation to pressure, did not occur until around 75kpa for the silicone muscles and 150kpa for Latex muscles ((b)

Figure 3.7).

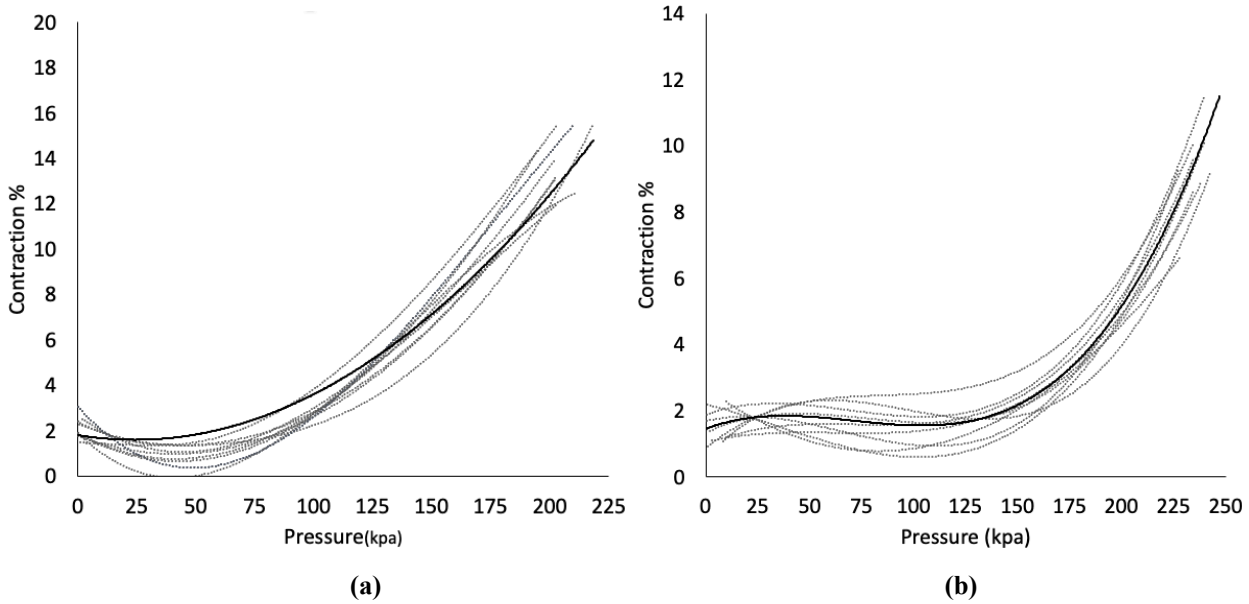

(a) **(b)**

Figure 3.7: Correlation between Pressure and Contraction of Latex and Silicone MKM muscles
Contraction percentage plotted against Pressure (kpa). Mean regression model (solid line) fitted to n=10 test trials (dotted lines) of silicone (left panel) and latex (right panel) MKM. The linear regression equation for the Silicone muscle is $y=0.0003x^2 -0.0169x +1.8216$ ($R2 = 0.7.085$). For the Latex muscle the linear regression equation $y=0.00002x^3-0.0004x^2+0.0237x+1.475$ ($R^2 = 0.708$).

3.4.2 Effect of Contraction on Tensile force

Similar general tensile force behavior was observed in both silicone and latex muscles (Figure 3.8). Overall there was positive almost near linear relationship between contraction and tensile force over a range of approximately 2 to 12 % contraction. However, this linear relationship did not continue as the max contraction was reached for both types of MKM muscles above 12 % contraction. A linear regression curve fit to silicone muscle contraction-tensile force behavior fit

well compared to the latex muscle force curves. Quantitatively, there was a greater peak tensile force-contraction relationship observed in the latex muscle at 14.608 N SE ±0.099 at a contraction of 9.418% SE± 0.580, compared to the silicone muscle. For the silicone muscle, there was a tensile force-contraction peak of 7.101 N SE± 0.068 at a contraction 13.23 % SE± 0.586.

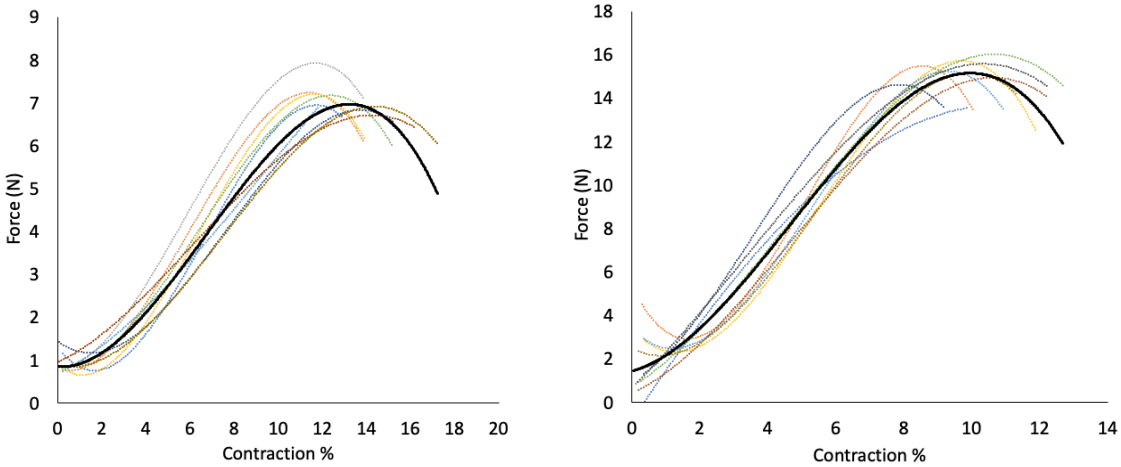

(a) **(b)**

Figure 3.8: Tensile force of Mckibben muscles
(a) 99mm silicone muscle $y=-0.0055x^3 + 0.1111x^2 - 0.0408x + 0.8588$ ($R^2 = 0.711$) (b) 113 latex muscle: Linear Regression equation $y = -0.0236x^3 + 0.3318x^2 + 0.4122x + 1.452$ ($R^2 = 0.5828$).

3.4.3 Effect of Contraction of Axial force

Compared to contractile force-contraction behavior, there was a similar positive relationship between axial force and contraction of the MKM. As the contraction of the MKM muscle increased, concomitantly axial force increased as well. In comparison, the latex muscle produced slightly greater peak axial force at 83.946 N SE ±0.612 in relation to the MKM producing 72.11 N SE ±0.695. However, the Silicone MKM had a peak contraction of 13.23 % SE ±0.586 compared to the Latex MKM's average peak contraction of 9.418% SE±0.580 (Figure 3.9). The linear regression model applied to the average contraction-axial force behavior plot fit accurately compared to a linear regression model fit producing an R^2 value of 0.5828.

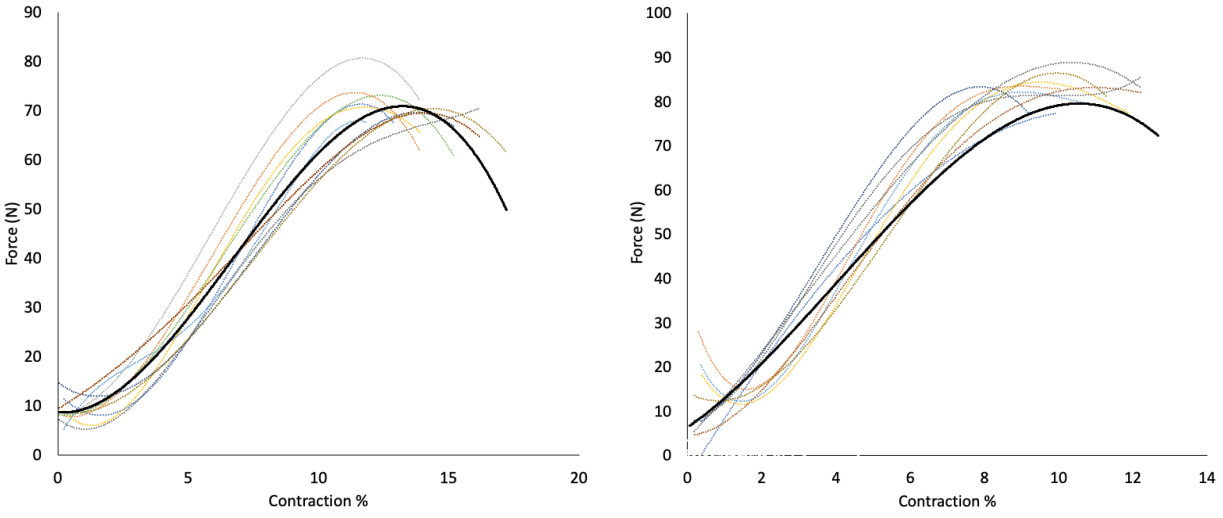

Figure 3.9: Axial force of Mckibben muscles
(a) 99mm silicone muscle $y=-0.0561x^3 + 1.1281x^2 + 0.3987x + 8.6813x$ (R2=0.7115) (b) 113 latex muscle: Linear Regression equation $y=-0.073x^3+ 0.879x^2 + 5.7835x + 6.379$ (R^2=0.5051)

3.4.4 Work efficiency of Latex and Silicone MKMs

In Figure 3.10 the average work efficiency was calculated based from twenty tests of each individual muscle. In total, four latex muscles and five silicone muscles were tested. Of all the Latex muscles tested, L1 had a minimum work efficiency value of 31.9% SE 0.225 and L3 had a maximum efficiency work value of 57.2% SE 0.14. In contrast, for the silicone MKM trials, S3 was the least efficient with an average efficiency value of 23.6% SE ±0.142 and S4 with a maximum average efficiciency of 41.8% SE± 0.166. Qualitatively, the latex MKMs had greater efficiency value compared to the Silicone MKMs (Fig. 2.2.6).

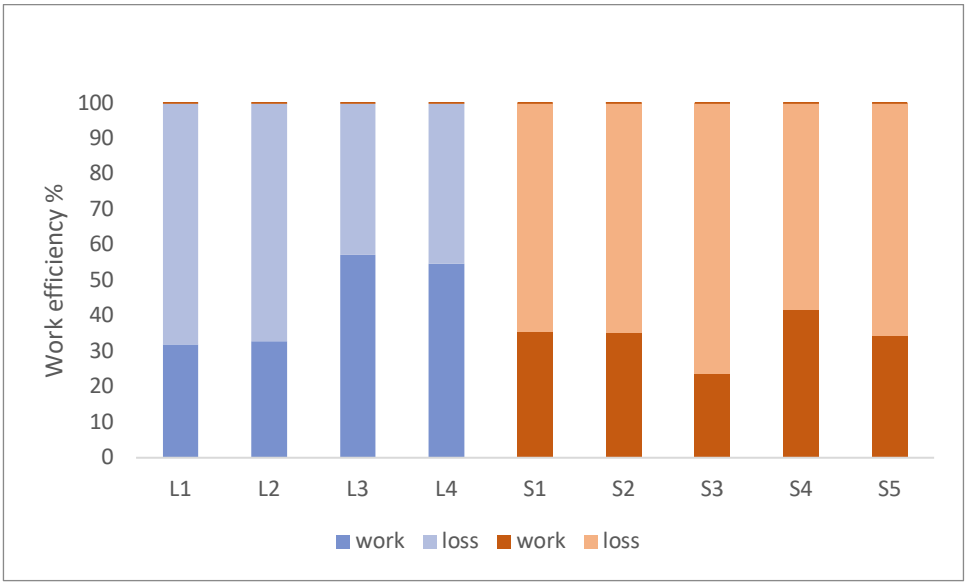

Figure 3.10: Work efficiency of Latex
(L1 – L4; each bar n=1) and Silicone (S1 – S5, n=5) MKM muscles. Darker colors represent work performed, and lighter color counterparts represent work loss.

3.5 Discussion

The testing of latex and silicone fabricated muscles revealed positive linear relationships between pressure, contraction, axial forces, and tension forces. After comparing contraction versus pressure average regression trendlines, it is apparent that latex MKM muscles could sustain a larger peak pressure than silicone MKMs (average peak pressure of 230 kpa, compared to the averaged 204 kpa of a silicone MKMs). Latex muscles consistently sustained higher pressures than silicone muscles which not a unique trend. In other studies latex muscles reached maximum pressures of 323 kpa were averaged in other latex trials, juxtaposed against a maximum of 307 kpa produced in Silicone MKM trials (Belk and Paulin, in prep).

3.5.1 Effect of differing Latex elasticity versus silicone elasticity

It was previously noted that it took considerably more pressure for the latex MKMs to begin contracting compared to Silicone MKMs (section 3.3.6). This difference in material quality may reflect the latex's higher Young's modulus: 0.001-0.0025GPa for Latex and 0.000845GPa for Smooth Sil940A silicone (Cambridge Engineering 1988). The Young's modulus is a measurement of the stiffness of a material; The higher the Young's modulus value, the stiffer and less pliant a

material. Additionally, the tensile strength, another mechanical property indicative of elasticity, of natural rubber (a.k.a latex) is a factor of ten higher (22-32MPa) compared to silicones (2.4-5.5 MPa). Latex's higher tensile strength possibly validates the increased pressure needed to contract a latex MKM. As a less-elastic material contracts, it would also exhibit higher inner-tension forces compared to more elastic materials.

When pressures are normalized, relatively, during contraction-tension relationships (Latex, 198.02 kpa $\pm$ 3.236 and silicone, 197.23 kpa $\pm$ 2.32), the latex tension force is roughly two times larger than Silicone values (Latex, 12.209 N $\pm$ 0.244 and Silicone, 6.859N $\pm$ 0.08). This relationship is demonstrated by the latex MKM's average tension force being almost double of the Silicone MKM's. One should bear in mind that an increase in tension force does not take into consideration a normalized pressure over the different media muscles. Furthermore, according to the average linear regression in figure 3.2.3, the Silicone MKM achieves a greater overall average displacement of 13.23mm versus latex's 10.03mm while the Silicone MKM operates at a peak pressure 30kpa lower than the latex MKM. In short, the Silicone muscle can operate at a lower pressure and contract more than the latex muscle.

3.5.2 Loaded Isotonic tests

In the original experiments four latex MKMs and five silicone MKMs were compared in isotonic tests under varying loads (Figure 3.7). Contractions were performed in an unloaded (zero) state, 1g, 5g, and 10g loaded states. For each loaded isotonic state, each muscle was tested five times. In total, each MKM underwent twenty loaded/unloaded isotonic tests. No significant change in contraction was noticed visually or quantitatively under each of the loads. After analyzing the isotonic loaded data it is apparent that the loads were not heavy enough. Past studies have conceptualized how a given MKM at a given pressure, will lengthen with added mass (Al-Ibadi et al. 2017; Daerden and Lefeber 2002).

3.5.3 Apparatus design improvement

The inconsistent data and lack of quality (time-contraction-pressure) affected this study. The muscles performed well, but variability in the data was attributed to the testing apparatus setup.

Before running through the laundry-list of problems, it should be emphasized that this lab was not equipped with suitable pneumatics data acquisition units found in other engineering/physics/materials labs.

The main reason for the variability in the work efficiency tests and lackluster contraction tests would be the junctions between the polyethylene hosing and MKM muscles. The junctions were tightened with cable ties to minimize leaking air from valves. Some of the valves were 3D printed and because of the layered manufacturing led to uneven valve surfaces. To correct this problem, all joints were sanded with fine-grit sandpaper and a second zip tie added to tighten the tube/joint seal. Results increased in efficiency by almost 30% (data not shown). However, the author still believes there could be air leaking from other joints (i.e. polyethylene tube-pressure sensor junctions) during isotonic load tests. Added mass on the underside of the MKM muscle only strains these joints, further increasing the chance of leaking air. Therefore, the work efficiency presented in this study can be refuted. In an ideal testing environment with 0% loss of air, the work efficiency of these muscles would be much higher. To further increase the efficiency of the testing system, each of the MKM muscles would be fitted with aluminum collars on either ends of the MKM muscles rather than with cable ties. In an ideal situation, future testing apparatuses would use air pumps, force gauges, and servo-controlled valves to control air in the closed system.

Reported maximum efficiency of the presented latex MKMs is 57.2% (Figure 3.2.6). These efficiency calculations are similar to the efficiency recordings of traditionally fabricated pneumatic MKMs reported by Meller et al. (2014). In Latex muscles inflated to 4.1 bar (410kpa) efficiency was reported to be 25%. In contrast, when these same MKMs were pressurized hydraulically, with fluid, efficiency increased to 60%. The higher calculated efficiencies of the latex MKMs in this study compared to Meller's reported efficiencies is promising. The MKMs tested in the Meller et al. study were approximately 14-17 cm in length compared to the presented MKM that are 5cm in length. The Meller et al. study reported contraction at approximately 20% at 3-4 bar (300-400kpa) in latex MKMs. For this study there was approximately 12% contraction at 250kpa in latex muscles. It begs the question whether the presented latex muscles could contract further at 300-400kpa.

3.5.4 Added measurement equipment

In future MKM studies, including a force gauge in the experimental setup would allow axial force and inner MKM membrane tension force to be measured separately. Currently the two force values are derived from pressure-based force equations (1 & 2). Because the two calculated force values are indirectly based on length and pressure values, the presented force models look similar. With additional force measuring equipment, axial forces could be measured independently and compared to these projected models.

Differences between theoretical and actual force plots could point out areas of improvement in future designs. Similar to Park & Wood's (2013) MKM design, a piece of resistive eGaIn wire and a liquid conductor, could be casted in the MKM to measure resistance, and tensile strength derived. Additionally, measuring resistance would help elucidate the non-linear behavior of MKMs, regardless of inner tube material. In past studies, dry friction between the sheath and elastomer tube has been responsible for presence of hysteresis during MKM inflation (Daerden and Lefeber 2002; Chou and Hannahford 1996). Additional data could demonstrate the lack of hysteresis in the MKM designs and would validate the integrated tube/mesh design.

3.5.5 Prototype MKM changes

The brush-on silicone/latex application is a quick and efficient method to produce MKM muscles. However, during fabrication and testing it was apparent that prototype MKM walls did not have a uniform thickness. This would have inevitably led to variable muscle contraction behavior during testing. In future prototypes, molding would be a more suitable fabrication method to ensure consistency. Also noted during the brush-on method was the tendency for micro-air bubbles to form in the curing latex (Belk and Paulin, in prep). These micro-bubbles contributed to a reduced MKM life, and the increase chance of the MKM skin rupturing under pressure. One unaddressed question during MKM analysis was: Do constricting MKM fibers, contracting due to increased pressure, tear into silicone/latex walls creating micro-chambers/bubbles susceptible to bursting? It became apparent that during testing some sheath fibers after successive inflation began to cut through the silicone walls. Tearing was more prevalent in silicone MKMs versus latex MKMs (Belk and Paulin, in prep). To avoid this in the future, plastic mesh could be coated in a thin release

agent before uncured silicone is applied. The release agent would act as a lubricant to minimize rubbing and eventual laceration of the MKM walls.

With the aforementioned flaws in both MKM prototype and testing apparatus designs addressed, monolithic-casted MKMs are still an area worth pursuing. These MKMs contract to similar degrees and are approximately as efficient as MKMs produced and tested in other studies (Meller et al. 2014). Other robotic studies have included these MKMs to actuate prototype hydraulic joints (Landkammer et al. 2014). In Landkammer's (2014) bioinspired spider joint, he integrated a pneumatic muscle into his bellowed design to rapidly flex his joint. In this study, the goal is to create and analyze the passive dynamics in a spider-like robot which does not require mechanisms for passive flexion, and because the polypropylene backbone is elastic, an integrated MKM would be redundant. However, to study leg gripping, and bouncing in a spider robot, it would be useful to integrate MKMs for joint flexion. Lateral movements in the tarsus and other spiders can be actuated by a dual antagonistic MKM apparatus operating from within the spider robot platform. The inclusion of MKMs in the spider robot are purely speculative. Even so, future investigation of these cheap MKM is worth pursuing. These inexpensive MKMs can easily be manufactured and incorporated into pneumatic robots to reduce weight and increase compliant activity.

4 Discussion

4.1 Conclusion

Locomotion is an adaptive behavior that allows an organism to interact with its environment efficiently while maximizing its survival and reproduction. When examined more closely, locomotion is a highly dynamic behavior determined and controlled by an interplay of the nervous system, the external environment, and body design. The nervous system is often treated as the primary controller of this adaptive system, interpreting input signals from the environment and finely tuning output signals to an animal's musculoskeletal system for gait adjustments, thus increasing efficiency (Bidaye et al. 2018). However, the nervous system is merely a contributing member. Biomechanically, an animal's mechanical design has evolved to move cyclically and rhythmically through an environment, recovering and storing energy in muscles and tendons. This mechanical system operates at a natural frequency that can be exploited by the central nervous system, requiring minimal neural control (Chiel and Beer 1997; Biewener 2003).

In the field of biomimetic robotics, capturing the passive dynamics, or the body's innate ability to recapture energy through a locomotive gait cycle and to minimize energy expenditure, has become a focus of academic research over the last three decades (McGeer 1990; Full and Koditschek 1999). Attention is now equally given to mechanical design and robot control systems, especially animal-mimicked robots. Similar to their biological counterparts, more biorobots now include compliant materials, rather than mechanical linkages, allowing them to be more dynamic and exhibit the similar viscoelastic-like properties of muscle and tendons. Furthermore, the field of biomimetic robots is paying more attention to insect-like robots for their versatility, stability, and robustness (Full et al. 1991; Landkammer et al. 2014; Zhu et al. 2014). Polypedal animal models such as the cockroach and spider, offer a stable platform from which to understand the relationship between control and the passive dynamics of biomechanical design. Spider mechanical design is a relatively unexplored field but could prove useful and integrative due to the spider's unique and powerful musculo-hydraulic actuated limbs.

My study follows the path of past investigations of emulating spider joints in robotic design (Nentwig 2013; Landkammer et al. 2014; Sprowitz et al. 2017). The design presented in my thesis represents a deviation from past spider models by attempting to emulate not only the hydraulic actuated joint, but the energy-saving properties of the leg as well. The monolithic leg design is compliant and mimics elastic components of the spider leg such as the transarticular sclerite (Sensenig and Shultz 2003).

The here presented leg includes and is bolstered by the current development of additive manufacturing and soft robotic technologies. Prototypes can now be quickly manufactured using 3D printers in a variety of materials which allows for the isolation of certain properties in individual components. Using the Dolomedes spider leg design as an example, I manufactured specific parts of the spider leg in either ABS or PP to specifically capture balance, compliance, and rigidity characteristics and to mimic the biological model as closely as possible. In addition, the rapid prototyping on the 3D printer allowed for refinement in pneumatic bladder design. For example, the extrusion diameter on the 3D printer was reduced to create fine-relief molds enabling smaller bladder size. Through the prototyping process, bladder size was the limiting factor on overall leg size. The presented study demonstrates how accurate dynamic models can be designed and fabricated based on biological models to further understand the underpinnings of animal locomotion.

4.2 Suggestions for future research

Two separate chapters are presented in this thesis, one related to integrated McKibben Muscles, and the other based on the mechanical design of a spider leg inspired by *Dolomedes aquaticus*. While two chapters may appear distinct and unrelated, my intention was to drive the movement of the spider robot using a combination of pressurized air cylinders and MKMs. When viewing a spider running from the side, the spider's leg gait cycle follows a roughly elliptical trajectory (Weihmann 2013). The lateral elements of this trajectory, viewed from an anterior to posterior position, could be articulated in a robotic system through an antagonistic setup of two MKMs. Alternatively, one MKM and spring could drive a rotary actuator attached to the trochanter of a

spider leg. To drive this entire pneumatic setup, Co2 cartridges would deliver air to pressurize the system.

In hindsight, and this will sound contrary to previously made statements in this theis, pneumatic muscles would not provide suitable torque nor the overall contraction to actuate a pneumatic spider leg roughly the size of the prototype presented in this thesis (Tavakoli et al. 2009). Pneumatic muscle are designed to reflect the behavior of biological muscle, but cannot be stretched or contracted to the same degree(Chou and Hannaford 1994). If a pneumatic muscle contracts only 10-20% of its resting length and is connected to a rotating spider leg, the translating travel angle of the leg would be less than if the spider leg had been actuated by an electrical rotary actuator (i.e. a motor). To apply a given torque or pulling force, electrical actuators are a lighter solution compared to pneumatic actuators (this includes the air supply to power the pneumatic actuator). Additionally, considering the geometrical constraints of a small robot, electrical actuators can fit into smaller spaces compared to pneumatic muscles which need comparably more space to accommodate the length of the muscle (Tavakoli et al. 2009). Bearing this information in mind, future spider models, especially built on a small scale, should favor integrating electrical actuators over pneumatic muscles.

Past studies have looked at the biomechanics and locomotive kinematics of the Chilean rose tarantula (*Grammistola rosea*), Brazilian tarantula (*Gramistola Mollicoma)*, and tiger wandering spider (*Cuppienius salei*)(Biancardi et al. 2011; Weihmann 2013; Hao et al. 2019). In comparison to *Dolomedes aquaticus,* all three spider species are much larger than *Dolomedes aquaticus*, although the *Cuppinienius salei* exhibits similar sit-and-wait behavior to Dolomedes species. Because of the difference in environment, size, and behavior, further investigation of the kinematics and ground reaction forces during locomotion of Dolomedes species compared to these other spider species, may be worth investigating. Biancardi et al. (2011)reported there was an estimated efficiency of locomotion of 4% in *Grammisola mollicoma*. If estimated efficiency of locomotion were calculated for smaller spider species such as Dolomedes, it could inform future research about the plausibility of the presence of other passive dynamic components in Dolomedes biomechanical design. In addition, stride frequency, center of mass position, and ground reaction forces could demonstrate whether there was pendulum-like energy exchange

during running or walking (Full and Tu 1990). Further, lateral, vertical and horizontal force vectors deduced from a combination of video and force plate data could inform control algorithms for a robotic spider leg.

Previously it was suggested that the aim of this thesis was to move away from a purely mechanically driven system. One advantage of mechanical systems over compliant systems is their robustness which allows for precise leg control (Ijspeert 2014). Indeed, compliant systems are dynamic, lightweight, and naturally dampen external forces. However, with increased dynamism and more play in the overall structure, compliant systems require more complex control schemes in place compared to mechanical systems. One prior goal of this thesis was to make a fully functional pneumatic robot that was energy efficient. With a nearly completed body, the other half of the locomotion equation needs to be addressed – the nervous system. The nervous system in this case would be a CPU with control algorithms that would take in sensory input from various external sensors (i.e. leg accelerometers, proprioceptors, and membrane resistance) and work in tandem with the body design to decrease overall energy expenditure.

4.3 Resonance in Mechanical systems

Systems and materials have a resonance frequency, i.e. a frequency where a body oscillates with little to no external input force (Ahlborn et al. 2006). Resonance can be achieved when an intermittent external force, at a given specific frequency (resonant frequency), results in the amplification of an intrinsic oscillation of that system. This resonance phenomena can also be applied to walking animals. When step frequency is tuned to the musculoskeletal system's natural frequency, this leads to a drop in elastic hysteresis in compliant tissues, thus saving energy. Mechanical energy, that is lost during the gait cycle of a walking animal is dissipated as heat (Cavagna and Legramandi 2015). Neuronal circuits termed central pattern generators use afferent input about environmental stimuli to tune rhythmic output firing signals to contract muscles in order to match the body's natural frequency. This tuning is referred to as entrainment (Zheng 2006).

Controllers that mimic biological central pattern generators can be included in biomimetic robots to provide synchronization of adaptive control modules and a robot's natural mechanical

frequency. It is important to keep in mind that biomimetic robots are designed to simulate biological systems, but not be exact imitations. Consequently, as mechanical systems, biomimetic robots will have their own individual natural frequencies different from the biological models (Cruse et al. 1995). Buchli et al. (2006) designed a quadruped robot with a controller that matched its oscillating output frequency to the robot's intrinsic frequency. Computationally, the controller used a series of coupled non-linear oscillators to modulate the controller frequency to rhythmic feedback input cycles. These adaptive frequency oscillators allowed the robot to change its behavior, according to constant updated feedback information.

Preliminary research into finding the presented spider leg's natural frequency was conducted in this study, but due to evidence and time constraints, was discontinued. These preliminary data are presented in the appendix (Apendix C). To determine and isolate the natural frequency of the presented spider leg, single-leg, three-legged, and six-legged models were built based on the findings of (Pullar and Paulin 2018) that the forelegs of *Dolomedes aquaticus* are used more for tactile sensing than locomotion. Hence, the gait characteristics of *Dolomedes aquaticus* are closer to a hexapedal alternating tripod gait. With an alternating tripod gait, three legs remain on the ground at all times. The legged models followed the finalized tubular Fusion 360 design but with a polypropylene core to make the leg more compliant. Initial observations of tripod motorized models indicate that motor revolutions can be tuned to match leg elastic recoil. In the future a simple feedback controller could be implemented into the tripod. By adjusting motor speed based on embedded accelerometer and joint resistance sensor feedback, proxies for leg extension and flexion, the multi-legged models' natural frequency can be amplified. Eventually, control policies could be implemented on a fully operational octopedal or hexapedal robot to adjust leg stiffness and gait frequency according to the ground substrate (tiled floor vs. carpet). Studying the passive dynamics of polypedal animals will open new avenues for both roboticists and biologists to better understand the dynamic connection between body design and the nervous system.

References

Ahlborn BK, Blake RW, Megill WM. 2006. Frequency tuning in animal locomotion. Zoology. 109(1):43–53. doi:10.1016/j.zool.2005.11.001.

Al-Ibadi A, Nefti-Meziani S, Davis S. 2017. Efficient structure-based models for the McKibben contraction pneumatic muscle actuator: The full description of the behaviour of the contraction PMA. Actuators. 6(4). doi:10.3390/act6040032.

Alexander M. 1996. Walking and Running. 80(488):262–266.

Alexander RM. 1991. Energy-saving mechanisms in walking and running. J Exp Biol. 160:55–69.

Altendorfer R, Moore N, Komsuoglu H, Buehler M, Brown HB, Mcmordie D, Saranli U, Full R, Koditschek DE. 2001. RHex: A biologically inspired hexapod runner. Auton Robots. 11(3):207–213. doi:10.1023/A:1012426720699.

Belforte G, Eula G, Ivanov A, Sirolli S. 2014. Soft pneumatic actuators for rehabilitation. Actuators. 3(2):84–106. doi:10.3390/act3020084.

Bensaude-Vincent B. 2011. A Cultural Perspective on Biomimetics. Adv Biomimetics. doi:10.5772/10546.

Bereiter C. 2009. Innovation in the absence of principled knowledge: The case of the wright brothers. Creat Innov Manag. 18(3):234–241. doi:10.1111/j.1467-8691.2009.00528.x.

Biancardi CM, Fabrica CG, Polero P, Loss JF, Minetti AE. 2011. Biomechanics of octopedal locomotion: kinematic and kinetic analysis of the spider Grammostola mollicoma. J Exp Biol. 214(20):3433–3442. doi:10.1242/jeb.057471. http://jeb.biologists.org/cgi/doi/10.1242/jeb.057471.

Bidaye SS, Bockemühl T, Büschges A. 2018. Six-legged walking in insects: How CPGs, peripheral feedback, and descending signals generate coordinated and adaptive motor rhythms. J Neurophysiol. 119(2):459–475. doi:10.1152/jn.00658.2017.

Biewener AA. 2003. Animal Locomotion. Oxford Univerity Press.

Blanes C, Mellado M, Beltran P. 2014. Novel additive manufacturing pneumatic actuators and mechanisms for food handling grippers. Actuators. 3(3):205–225. doi:10.3390/act3030205.

Blickhan R. 1989. The Spring-Mass Model for Running and Hopping. Jounal Biomech. 22(11):1217–1227.

Blickhan R, Barth FG. 1985. Strains in the exoskeleton of spiders. J Comp Physiol A. 157(1):115–147. doi:10.1007/BF00611101.

Blickhan R, Seyfarth A, Geyer H, Grimmer S, Wagner H, Günther M. 2007. Intelligence by mechanics. Philos Trans R Soc A Math Phys Eng Sci. 365(1850):199–220. doi:10.1098/rsta.2006.1911.

Buchli J, Iida F, Ijspeert AJ. 2006. Finding resonance: Adaptive frequency oscillators for dynamic legged locomotion. IEEE Int Conf Intell Robot Syst.:3903–3909. doi:10.1109/IROS.2006.281802.

Cambridge Engineering. 1988. Materials data Book. Mater Des. 9(5):305. doi:10.1016/0261-3069(88)90026-x.

Cavagna GA, Heglund NC, Taylor CR. 1977. Mechanical work in terrestrial locomotion: two basic mechanisms for minimizing energy expenditure. Am J Physiol - Regul Integr Comp Physiol. 2(3). doi:10.1152/ajpregu.1977.233.5.r243.

Cavagna GA, Legramandi MA. 2015. Running, hopping and trotting: Tuning step frequency to the resonant frequency of the bouncing system favors larger animals. J Exp Biol. 218(20):3276–3283. doi:10.1242/jeb.127142.

Chiel HJ, Beer RD. 1997. The brain has a body: Adaptive behavior emerges from interactions of nervous system, body and environment. Trends Neurosci. 20(12):553–557. doi:10.1016/S0166-2236(97)01149-1.

Chou CP, Hannaford B. 1994. Static and dynamic characteristics of McKibben pneumatic artificial muscles. Proc - IEEE Int Conf Robot Autom.(pt 1):281–286. doi:10.1109/robot.1994.350977.

Chou CP, Hannaford B. 1996. Measurement and modeling of McKibben pneumatic artificial muscles. IEEE Trans Robot Autom. 12(1):90–102. doi:10.1109/70.481753.

Chyou T, Liddell GF, Paulin MG. 2011. An upper-body can improve the stability and efficiency of passive dynamic walking. J Theor Biol. 285(1):126–135. doi:10.1016/j.jtbi.2011.06.032. http://dx.doi.org/10.1016/j.jtbi.2011.06.032.

Collins S, Ruina A, Tedrake R, Wisse M. 2005. Efficient bipedal robots based on passive-dynamic walkers. Science (80-). 307(5712):1082–1085. doi:10.1126/science.1107799.

Collins SH, Ruina A. 2005. A bipedal walking robot with efficient and human-like gait. Proc - IEEE Int Conf Robot Autom. 2005(April):1983–1988. doi:10.1109/ROBOT.2005.1570404.

Cruse H, Bartling C, Cymbalyuk G, Dean J, Dreifert M. 1995. A modular artificial neural net for controlling a six-legged walking system. Biol Cybern. 72(5):421–430. doi:10.1007/BF00201417.

Daerden F, Lefeber D. 2002. Pneumatic artificial muscles: Actuators for robotics and automation. Eur J Mech Environ Eng. 47(1):11–21. doi:10.1109/aim.2001.936758.

Van Damme M, Daerden F, Lefeber D. 2005. A pneumatic manipulator used in direct contact with an operator. Proc - IEEE Int Conf Robot Autom. 2005(April):4494–4499. doi:10.1109/ROBOT.2005.1570812.

Delcomyn F. 1980. Neural basis of rhythmic behavior in animals. Science (80-). 210(4469):492–498. doi:10.1126/science.7423199.

Dickinson MH, Farley CT, Full RJ, Koehl MAR, Kram R, Lehman S. 2000. How animals move: An integrative view. Science (80-). 288(5463):100–106. doi:10.1126/science.288.5463.100.

Dzahir MAM, Yamamoto SI. 2019. Dynamic modeling of McKibben muscle using empirical model and particle swarm optimization method. Appl Sci. 9(12). doi:10.3390/app9122538.

Ekeberg Ö. 1993. A combined neuronal and mechanical model of fish swimming. Biol Cybern. 69(5–6):363–374. doi:10.1007/BF01185408.

Ellis. 1944. The Mechanism of Extension in the Legs of Spiders Author (s): C . H . Ellis Published by : The University of Chicago Press in association with the Marine Biological Stable URL : https://www.jstor.org/stable/1537950. Biol Bull. 86(1):41–50.

Elsayed Y, Vincensi A, Lekakou C, Geng T, Saaj CM, Ranzani T, Cianchetti M, Menciassi A. 2014. Finite Element Analysis and Design Optimization of a Pneumatically Actuating Silicone Module for Robotic Surgery Applications. Soft Robot. 1(4):255–262. doi:10.1089/soro.2014.0016.

Fish FE, Lauder GV. 2006. Passive and Active Flow Control By Swimming Fishes and Mammals. Annu Rev Fluid Mech. 38(1):193–224. doi:10.1146/annurev.fluid.38.050304.092201. http://www.annualreviews.org/doi/10.1146/annurev.fluid.38.050304.092201.

Foelix RF. 1983. Biology of Spiders. Insect Syst Evol. doi:10.1163/187631283X00371.

Forster R, Forster LM. 1973. New Zealand Spider: An Introduction. Collins, Auckland.

Full RJ, Tu MS. 1990. Mechanics of six-legged runners. 146:129–146.

Full RJ. 2009. Learning from the gecko's tail.

Full RJ, Blickhan R, Ting LH. 1991. Leg design in hexapedal runners. J Exp Biol. 158:369–390. doi:10.1016/S0924-0136(97)00067-8.

Full RJ, Koditschek DE. 1999. Templates and anchors: neuromechanical hypotheses of legged locomotion on land. J Exp Biol. 202:3325–3332.

Gao Z, Shi Q, Fukuda T, Li C, Huang Q. 2019. An overview of biomimetic robots with animal behaviors. Neurocomputing. 332:339–350. doi:10.1016/j.neucom.2018.12.071.

Gasparetto A, Vidoni R, Seidl T. 2008. Kinematic study of the spider system in a biomimetic perspective. 2008 IEEE/RSJ Int Conf Intell Robot Syst IROS.:3077–3082. doi:10.1109/IROS.2008.4650677.

Gordon KE, Sawicki GS, Ferris DP. 2006. Mechanical performance of artificial pneumatic muscles to power an ankle-foot orthosis. J Biomech. 39(10):1832–1841. doi:10.1016/j.jbiomech.2005.05.018.

Goyen P. 1887. Descriptions on new species of New Zealand Araneae. Trans Proc New Zeal Inst. 63.

De Greef A, Lambert P, Delchambre A. 2009. Towards flexible medical instruments: Review of flexible fluidic actuators. Precis Eng. 33(4):311–321. doi:10.1016/j.precisioneng.2008.10.004.

Halsey LG. 2016. Terrestrial movement energetics: current knowledge and its application to the optimising animal. J Exp Biol. 219(10):1424–1431. doi:10.1242/jeb.133256. http://jeb.biologists.org/lookup/doi/10.1242/jeb.133256.

Hao X, Ma W, Liu C, Li Y, Qian Z, Ren Luquan, Ren Lei. 2019. Analysis of Spiders' Joint Kinematics and Driving Modes under Different Ground Conditions. Appl Bionics Biomech. 2019. doi:10.1155/2019/4617212.

Harrison P. 1992. Descartes on Animals. Philospohical Q. 42(167):219–227.

Hill AV. 1938. The heat of shortening and the dynamic constants of muscle. Proc R Soc London Ser B - Biol Sci. 126(843):136–195. doi:10.1098/rspb.1938.0050.

Hill AV. 2018. The mechanics of active muscle. 136(884):399–420.

Hirose S, Kato K. 2000. Study on quadruped walking robot in Tokyo Institute of Technology - past, present and future. Proc - IEEE Int Conf Robot Autom. 1:414–419. doi:10.1109/robot.2000.844091.

Ijspeert AJ. 2008. Central pattern generators for locomotion control in animals and robots: A review. Neural Networks. 21(4):642–653. doi:10.1016/j.neunet.2008.03.014.

Ijspeert AJ. 2014. Biorobotics: Using robots to emulate and investigate agile locomotion. Science (80-). 346(6206):196–203. doi:10.1126/science.1254486.

Ijspeert AJ, Crespi A, Cabelguen J. 2005. Simulation and Robotics Studies of Salamander Locomotion. Neuroinformatics. 3:175–195. doi:10.1385/NI. http://www.springerlink.com/index/X74873723718574K.pdf.

Ijspeert AJ, Crespi A, Ryczko D, Cabelguen J. 2007. From Swimming to Walking with a Spinal Cord Model. Science (80-). 315(5817):1416–1420. doi:10.1126/science.1138353.

Jayaram K, Full RJ. 2016. Cockroaches traverse crevices, crawl rapidly in confined spaces, and inspire a soft, legged robot. Proc Natl Acad Sci U S A. 113(8):E950–E957. doi:10.1073/pnas.1514591113.

Karner M. 1998. Restrictions in the evolution of arthropod joints. Biol Technol Walk. 375:18–24.

Kaston BJ. 1965. Some little known aspects spider behaviour. Am Midl Nat. 73(2):336–356.

Kim T, Member S, Yoon SJ, Park Y. 2018. Soft Inflatable Sensing Modules for Safe and Interactive Robots. IEEE Robot Autom Lett. 3(4):3216–3223. doi:10.1109/LRA.2018.2850971.

Klute GK, Czerniecki JM, Hannaford B. 1999. McKibben artificial muscles: Pneumatic actuators with biomechanical intelligence. IEEE/ASME Int Conf Adv Intell Mechatronics, AIM.:221–226. doi:10.1109/aim.1999.803170.

Klute GK, Czerniecki JM, Hannaford B. 2002. Artificial muscles: Actuators for biorobotic systems. Int J Rob Res. 21(4):295–309. doi:10.1177/027836402320556331.

Landkammer S, Schneider D, Winter F, Hess P, Hornfeck R. 2015. Static modeling of antagonistic pneumatic actuator for robotic applications. Proc 2015 IEEE Int Work Electron Control Meas Signals their Appl to Mechatronics, ECMSM 2015. doi:10.1109/ECMSM.2015.7208684.

Landkammer S, Valek R, Hornfeck R. 2014. A novel bio-inspired fluidic actuator for robotic applications. ICAST 2014 - 25th Int Conf Adapt Struct Technol.:1–11.

Landkammer S, Winter F, Schneider D, Hornfeck R. 2016. Biomimetic Spider Leg Joints: A Review from Biomechanical Research to Compliant Robotic Actuators. Robotics. 5(3):15. doi:10.3390/robotics5030015. http://www.mdpi.com/2218-6581/5/3/15.

Margolius I. 2017. The Robot of Prague. (17). https://czechfriends.net/images/RobotsMargoliusJul2017.pdf.

McGreer T. 1990. Passive Dynamic Walking. :62–82.

McKeown KC. 1935. Spider Wonder of Australia.

Meller MA, Bryant M, Garcia E. 2014. Reconsidering the McKibben muscle: Energetics, operating fluid, and bladder material. J Intell Mater Syst Struct. 25(18):2276–2293. doi:10.1177/1045389X14549872.

Menon C, Lira C. 2006. Active articulation for future space applications inspired by the hydraulic system of spiders. Bioinspiration and Biomimetics. 1(2):52–61. doi:10.1088/1748-3182/1/2/003.

Meyer J, Guillot A. 2008. Biologically I 60. Springer Handb Robot.:1395–1422.

Monk T, Paulin MG. 2014. Predation and the origin of neurones. Brain Behav Evol. 84(4):246–261. doi:10.1159/000368177.

Moya-Laraño J, Vinković D, De Mas E, Corcobado G, Moreno E. 2008. Morphological evolution of spiders predicted by pendulum mechanics. PLoS One. 3(3):1–6. doi:10.1371/journal.pone.0001841.

Nentwig W. 2013. Spider ecophysiology. Spider Ecophysiol.(January 2013):1–529. doi:10.1007/978-3-642-33989-9.

Neveln ID, Bai Y, Snyder JB, Solberg JR, Curet OM, Lynch KM, MacIver MA. 2013. Biomimetic and bio-inspired robotics in electric fish research. J Exp Biol. 216(13):2501–2514. doi:10.1242/jeb.082743. http://jeb.biologists.org/cgi/doi/10.1242/jeb.082743.

Nickel VL, Perry J, Garrett AL. 1963. Development of Useful Function in the Severely Paralyzed Hand. J Bone Joint Surg Am. 45(July):933–952. doi:10.2106/00004623-196345050-00004.

Park YL, Wood RJ. 2013. Smart pneumatic artificial muscle actuator with embedded microfluidic sensing. Proc IEEE Sensors.:1–4. doi:10.1109/ICSENS.2013.6688298.

Parry BY, Brown RH. 1959. The Hydraulic Mechanism of the Spider Leg. J Exp Biol. 36(2):423–433.

Pauslon LD. 2004. Biomimetic Robots. IEEE Trans Robot Autom. 37(9):48–53.

Petrunkevitch A. 1909. Contributions to our knowledge of the anatomy and relationships of spiders. Ann Ent Soc Amer. 2:11–21.

Pfeifer R, Scheier C. 2007. How the Body Shapes the Way We Think: A New View of Intelligence. Cambridge, MA: MIT Press.

Prusa Research. 2018. Prusa MK3 to MMU2 Guide. https://help.prusa3d.com/en/category/original-prusa-i3-mk3s-to-mmu2s_288.

Pullar K, Paulin M. 2018. Markerless tracking suggests a tactile sensing role for forelegs of Dolomedes spiders during locomotion. bioRxiv.:398479. doi:10.1101/398479.

Raibert M, Blankespoor K, Nelson G, Playter R. 2008. Big Dog, The Rough-Terrain Quadruped Robot. In: The International Federation of Automatic Control. IFAC. http://dx.doi.org/10.3182/20080706-5-KR-1001.01833.

Raibert MH. 1986. Legged Robots That Balance. Cambridge, MA: MIT Press.

Reußenzehn S. 2010. Mechanical design of the legs of Dolomedes aquaticus. (June).

Rottner R. 2019. Balloon background. http://www.madehow.com/Volume-2/Balloon.html.

Saibene F, Minetti AE. 2003. Biomechanical and physiological aspects of legged locomotion in humans. Eur J Appl Physiol. 88(4):297–316. doi:10.1007/s00421-002-0654-9.

Sensenig AT, Shultz JW. 2003. Mechanics of cuticular elastic energy storage in leg joints lacking extensor muscles in arachnids. J Exp Biol. 206(4):771–784. doi:10.1242/jeb.00182.

Sensenig AT, Shultz JW. 2006. Mechanical Energy Oscillations During Locomotion in the Harvestman Leiobunum Vittatum (Opiliones). J Arachnol. 34(3):627–633. doi:10.1636/0161-8202(2006)034[0627:meodli]2.0.co;2.

Seok S, Wang A, Chuah MY, Otten D, Lang J, Kim S. 2013. Design principles for highly efficient quadrupeds and implementation on the MIT Cheetah robot. Proc - IEEE Int Conf Robot Autom.:3307–3312. doi:10.1109/ICRA.2013.6631038.

Sfakiotakis M, Tsakiris DPÃ. 2007. Neuromuscular control of reactive behaviors for undulatory robots. 70:1907–1913. doi:10.1016/j.neucom.2006.10.139.

Shultz JW. 1991. Evolution of locomotion in arachnida: The hydraulic pressure pump of the giant whipscorpion, Mastigoproctus Giganteus (Uropygi). J Morphol. 210(1):13–31. doi:10.1002/jmor.1052100103.

Sinha A, Caer C, Petersen K, Sitti M. 2017. Scalable Pneumatic and Tendon Driven Robotic Joint Inspired by Jumping Spiders 4 ,¨. :0–6.

Sprowitz A, Gottler C, Sinha A, Caer C, Ooztekin MU, Petersen K, Sitti M. 2017. Scalable pneumatic and tendon driven robotic joint inspired by jumping spiders. Proc - IEEE Int Conf Robot Autom.:64–70. doi:10.1109/ICRA.2017.7988692.

Spröwitz A, Tuleu A, Vespignani M, Ajallooeian M, Badri E, Ijspeert AJ. 2013. Towards dynamic trot gait locomotion: Design, control, and experiments with Cheetah-cub, a compliant quadruped robot. Int J Rob Res. 32(8):932–950. doi:10.1177/0278364913489205.

Surentu J, Tuijthof GJM, Herder JL. 2007. Optimized artificial muscles for an inherently safe robotic arm. 2007 IEEE 10th Int Conf Rehabil Robot ICORR'07.(July):1070–1076. doi:10.1109/ICORR.2007.4428556.

Tavakoli M, Marques L, De Almeida AT. 2009. A comparison study on pneumatic muscles and electrical motors. 2008 IEEE Int Conf Robot Biomimetics, ROBIO 2008.(May 2014):1590–1594. doi:10.1109/ROBIO.2009.4913238.

Tondu B, Lopez P. 2000. Artificial Muscle Ro bot Act u ato r s. Control Syst. 20(2):15–38.

Tytell ED, Holmes P, Cohen AH. 2011. Spikes alone do not behavior make: Why neuroscience needs biomechanics. Curr Opin Neurobiol. 21(5):816–822. doi:10.1016/j.conb.2011.05.017. http://dx.doi.org/10.1016/j.conb.2011.05.017.

Villegas D, Van Damme M, Vanderborght B, Beyl P, Lefeber D. 2012. Third-generation pleated pneumatic artificial muscles for robotic applications: Development and comparison with Mckibben muscle. Adv Robot. 26(11–12):1205–1227. doi:10.1080/01691864.2012.689722.

Weihmann T. 2013. Crawling at High Speeds: Steady Level Locomotion in the Spider Cupiennius salei-Global Kinematics and Implications for Centre of Mass Dynamics. PLoS One. 8(6). doi:10.1371/journal.pone.0065788.

Williams DS. 1981. The feeding behaviour of new zealand dolomedes species (Araneae: Pisauridae). New Zeal J Zool. 6(1):95–105. doi:10.1080/03014223.1979.10428352.

Wirekoh J, Valle L, Pol N, Park YL. 2019. Sensorized, Flat, Pneumatic Artificial Muscle Embedded with Biomimetic Microfluidic Sensors for Proprioceptive Feedback. Soft Robot. 6(6):768–777. doi:10.1089/soro.2018.0110.

Zheng TIM. 2006. Sensory feedback mechanism underlying entrainment. :245–261. doi:10.1007/s00422-005-0047-3.

Zhu YG, Jin B, Li W, Li ST. 2014. Optimal design of hexapodwalking robot leg structure based on energy consumption andworkspace. Trans Can Soc Mech Eng. 38(3):305–317. doi:10.1139/tcsme-2014-0022.

Appendix A

Following are a set of three figures meant to provide supplementary information to Chapter 1. The figures describe a body of work including actuated joint and polypedal mechanical design that led to the presented spider pneumatic leg.

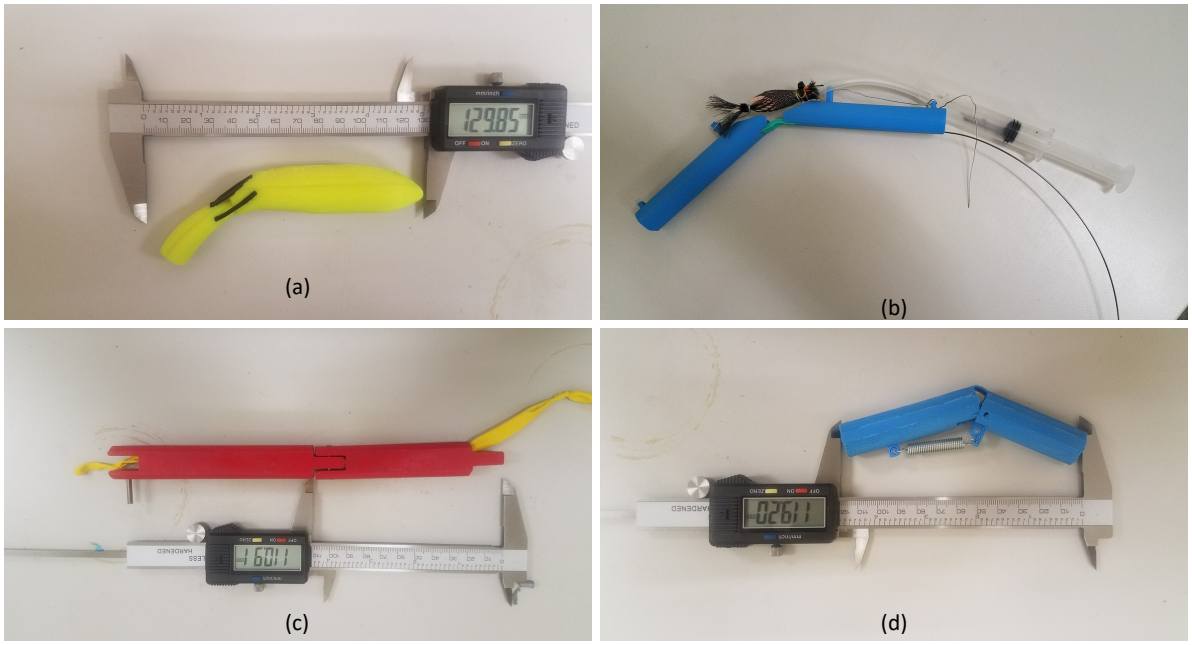

A.1 : Early joint designs
(a) Femur-patella joint printed from an STL directly modeled based the Dolomedes aquaticus CT-micro scan. Three black TPU bracings control lateral and vertical joint movement. (b) Pneumatic MKM joint design. As the syringe plunger is depressed, the MKM inflates leading to joint extension. A bent piece of "piano wire", high carbon steel wire, runs down the ventral side of the joint through a TPU joint, and counteracts the inflated MKM, providing the return elastic return force back to the joint's natural position. (c) Hinge joint with extension controlled by an inflated balloon (yellow). (d) Conceptual hinge joint with antagonistic spring mounted on the ventral side of the joint.

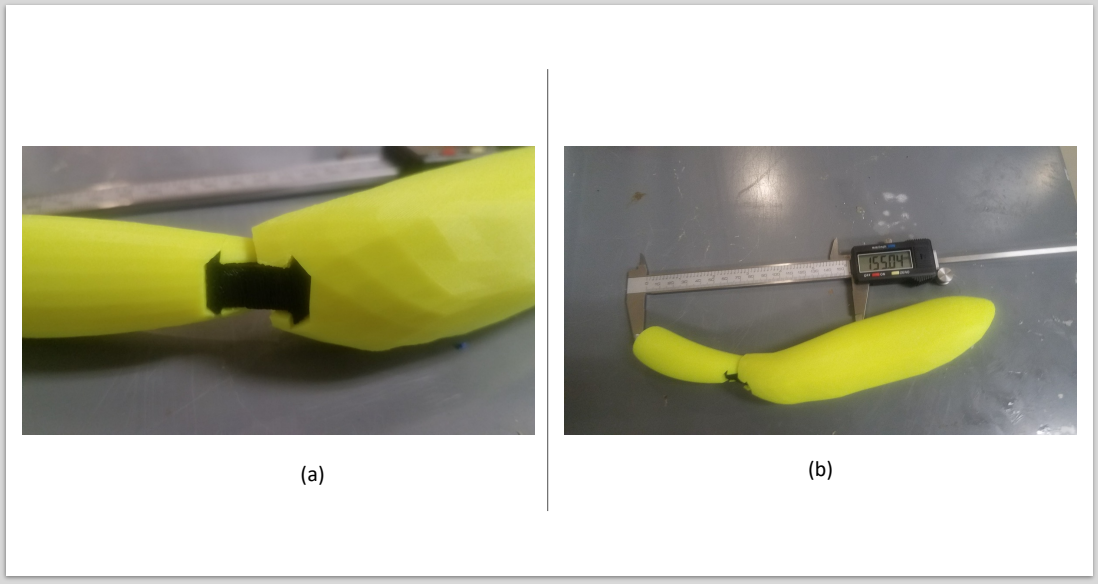

A.2 :Locking TPU joint design
Femur-patella joint printed in ABS based on the Dolomedes aquaticus micro-CT scan. The locking joint is printed in TPU, a flexible filament.

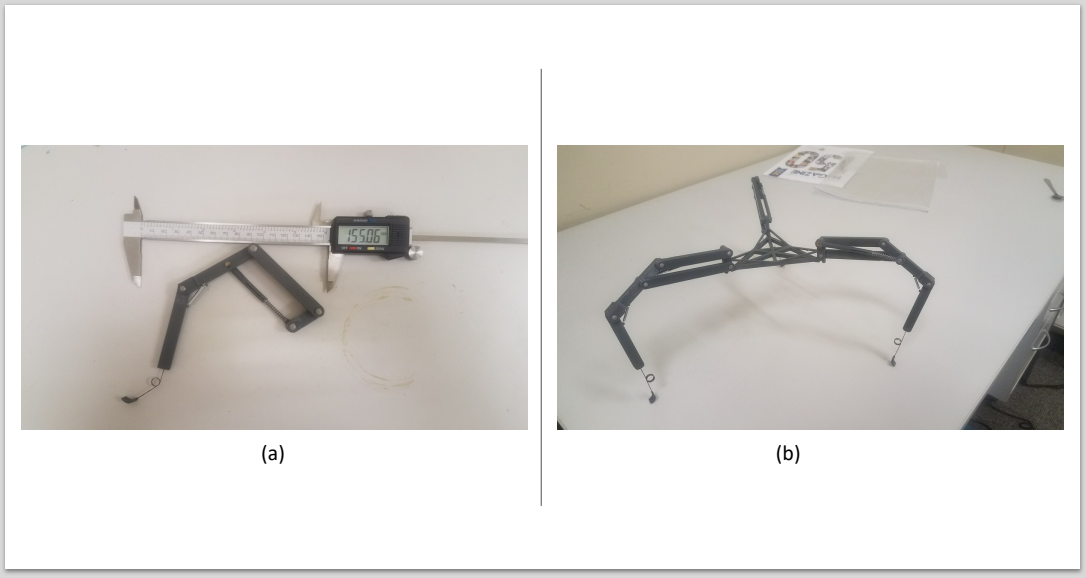

A.3 :Leg design and bouncing tripod design.
(a) Leg design inspired by Spröwitz et al.'s (2013) cheetah cub design. The traditional six segment design is reduced to a five-segment leg with an integrated compression spring - pantograph mechanism. A tension spring is also included to limit leg extension. The fifth segment, comparable to the spider leg tarsus, is connected to the segment assemblage by a torsion spring to dampen impact forces. (b) Tripod model with three spring legs

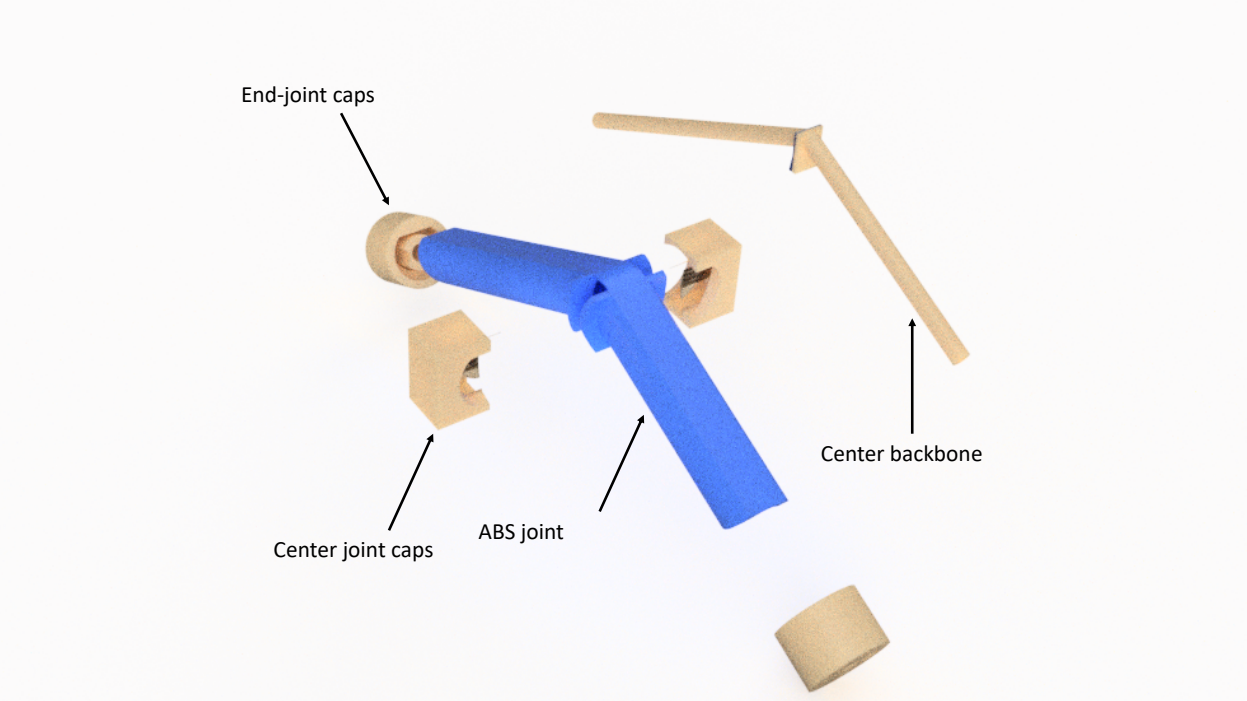

A.4 Illustration of the phase of fabricating the experimental silicone joint.
The center backbone, joint caps, and end caps are all made of BVOH, a water dissolvable material.

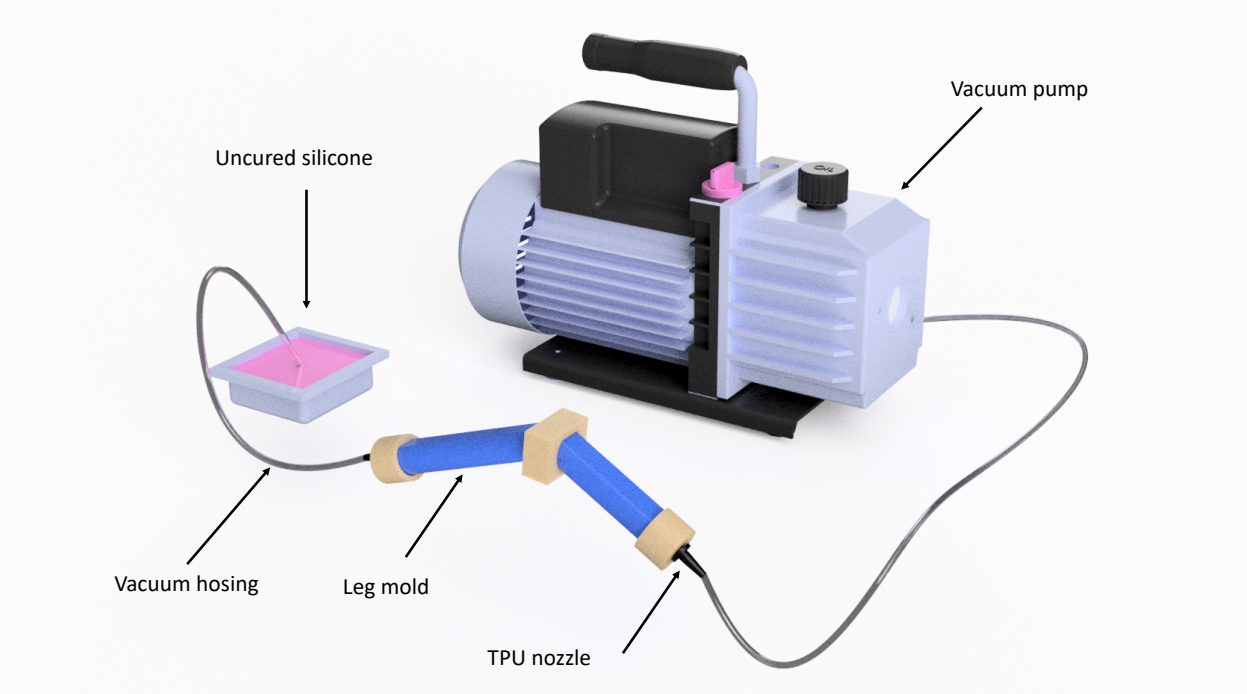

A.5 : Visualization of the second phase of fabricating the experimental silicone joints.
Negative pressure from the vacuum pump drew uncured silicone through hosing into the mold.

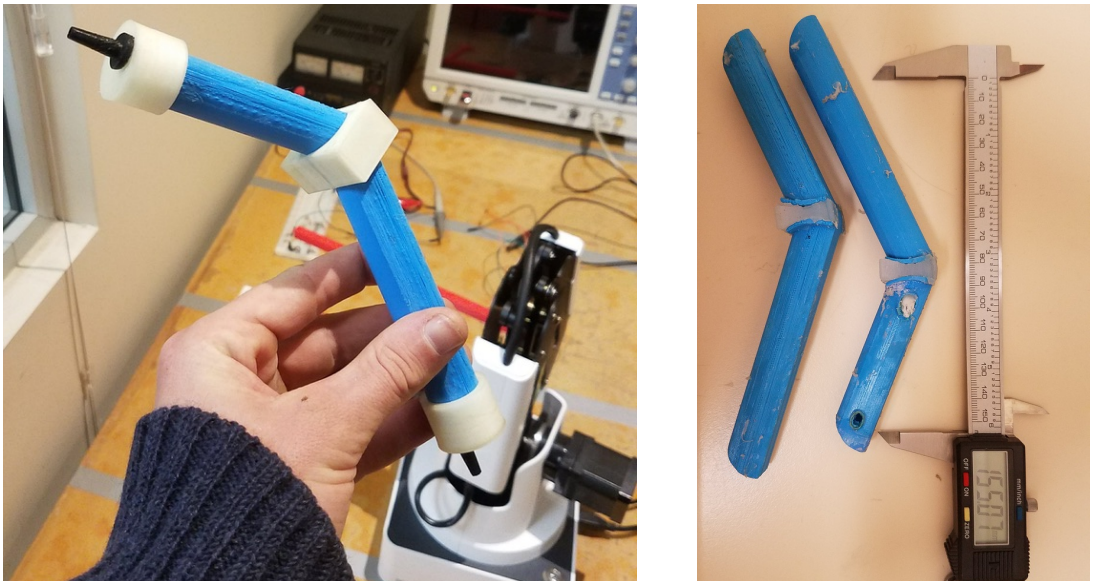

(a) (b)

A.6 : Before and after photos of phase two of silicone joint fabrication.
(a) Full joint setup with BVOH caps. (b) Joints with casted silicone bladder after the BVOH caps and backbone had been dissolved in hot water.

(a) (b)

A.7 : Construction of MMU2 addon for the Prusa MK3 printer.
(a)The Prusa MK3 single colour printer was supplied completely built. (b) The MMU2 (Multi material upgarade 2) is a second generation multi-filament print head that enables the MK3 to print objects in five different types of filament. Construction and calibration of the multi-filament printer took a significant amount of time and MK2 firmware was constantly updated as new software was released by Prusa Research. Both the multi-filament print head and main extrusion filament head contain pinda sensors (Prusa induction autoleveling sensor) that needed to be calibrated before printing (Prusa Research 2018).

Appendix B

Arduino Source Code for Pressure Sensor and ToF

```
#include "Adafruit_VL53L0X.h"
Adafruit_VL53L0X lox = Adafruit_VL53L0X();
void setup() {
 Serial.begin(115200);
  // wait until serial port opens for native USB devices
  while (! Serial) {
    delay(1);
  }
  Serial.println("Adafruit VL53L0X test");
  if (!lox.begin()) {
    Serial.println(F("Failed to boot VL53L0X"));
    while(1);
  }
  // power
  Serial.println(F("VL53L0X API Simple Ranging example\n\n"));
}
void loop() {
const int pinVplus = A0;
const int pinVmin = A1;
const float offset = 0.0;       // 0.0 for now, adjust this.  ...
  #define NUM_SAMPLES 20
int sumPlus = 0;
for( int i=0; i<NUM_SAMPLES; i++)
  sumPlus += analogRead ( pinVplus );
float vPlus = ((float) sumPlus / (float) NUM_SAMPLES ) / 1023.0 * 5.0;
  float vMin = (float) analogRead( pinVmin) / 1023.0 * 5.0;
  //Serial.print( F("vPlus[V]="));
  //Serial.println( vPlus, 4);
  //Serial.print( F("vMin[V]="));
  //Serial.println( vMin, 4);
  float diff = vPlus - vMin;
  diff -= offset;
  //Serial.print( F("diff[V]="));
  //Serial.println( diff, 4);
  // 0.2mV per kPa at 10V.
  // Assume 0.1mV per kPa at 5V.
  // Since the 'diff' is a float in volt, the pressure is 1/0.1mV times the diff.
  // So if the voltage changes 1 mV the pressure changes 10 kPa.
  float pressure = (diff / 0.0001)/6.2707;       // 0.0001 is 0.1mV
  //Serial.print( F("pressure[kPa]="));
  Serial.print("Pressure kpa:.....                                    ");
  Serial.println(pressure,4);
  VL53L0X_RangingMeasurementData_t measure;
  Serial.print("Reading a measurement... ");
  lox.rangingTest(&measure, false); // pass in 'true' to get debug data printout
  if (measure.RangeStatus != 4) {  // phase failures have incorrect data
    Serial.print("Distance (mm): "); Serial.println(measure.RangeMilliMeter);
  } else {
    Serial.println(" out of range "); }

  delay(100)
```

Appendix C

The following appendix is dedicated to a short summary of preliminary investigations analyzing oscillatory activity in *Dolomedes aquaticus*, and actuated compliant designs that mimic this behavior.

The Dolomedes locomotive pattern follows a variation of a hexapedal stepping pattern called an alternating tripod gait. It is important to note that *Dolomedes aquaticus* does have eight legs but its two front legs play a larger role in sensory perception (Pullar and Paulin 2018). An alternating tripod gait can be described as an out-of-phase pair of three-legged tripods. As a spider walks, one tripod set remains relatively stationary, while the other tripod set swings in an aft-fore direction. Once the tripod set completes a full step cycle, and makes contact with the ground, the tripods exchange, and the second tripod set moves forward (Figure A.10-A.11).

Initially the goal was to create a model simulating the oscillation of a single tripod group, and later on create a second model comprised of connected out of phase tripods. The leg design had to be modified and scaled down from the pneumatic leg presented in chapter 1. The final design featured a miniature Dolomedes leg with a polypropylene core that was stiff yet flexible.

The tripod displayed pendulum-like behavior (i.e. the center of mass had to oscillate left to right with a cyclic exchange of kinetic energy to potential energy and back to kinetic energy). Several designs were designed and trialed to simulate this “swaying” behavior. Early in the process of designing this oscillating model, it became clear that in order to elicit this swaying motion the pendulum would have to aggressively throw its weight from side to side. An inverted pendulum was experimented with but projected the model’s COM to high leading to wobbly, unsteady oscillations. Motors of varying sizes were attached to the tripod models, from 6V brushless electric motors down to micro-stepper motors. The motor had to have a balance of weight and power, so as not to compromise pendulum frequency and force, but also to avoid weighing down the model with excessive weight. Additional weight in the model would have impeded its ability to oscillate.

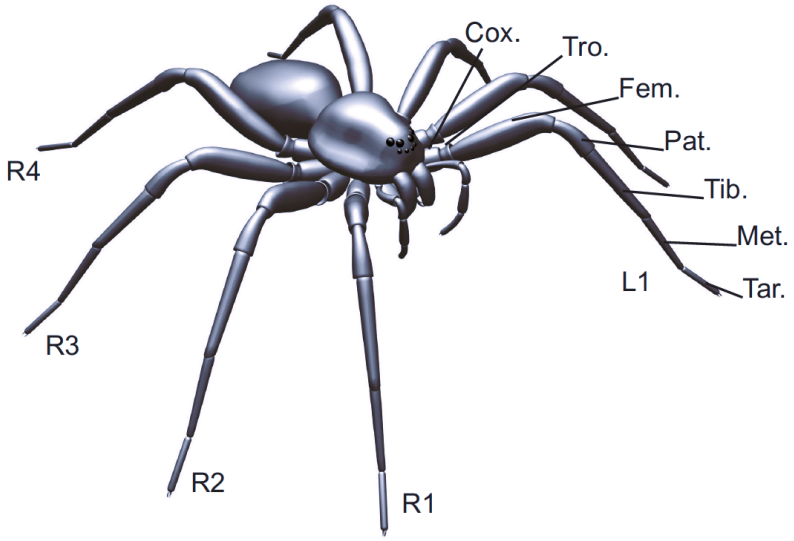

A.8 :3D model of *Dolomedes aquaticus* showing external anatomy.
The leg is broken down into its individual segments: Cox: coxa, Tro: trochanter, Fem: femur, Pat: patella, Tib: tibia, Met: metatarsus, Tar: tarsus. Legs are labelled as: R1: first on the right side, R2: second leg on the right side, L1: first leg on the left side, etc. (Reußenzehn 2010)

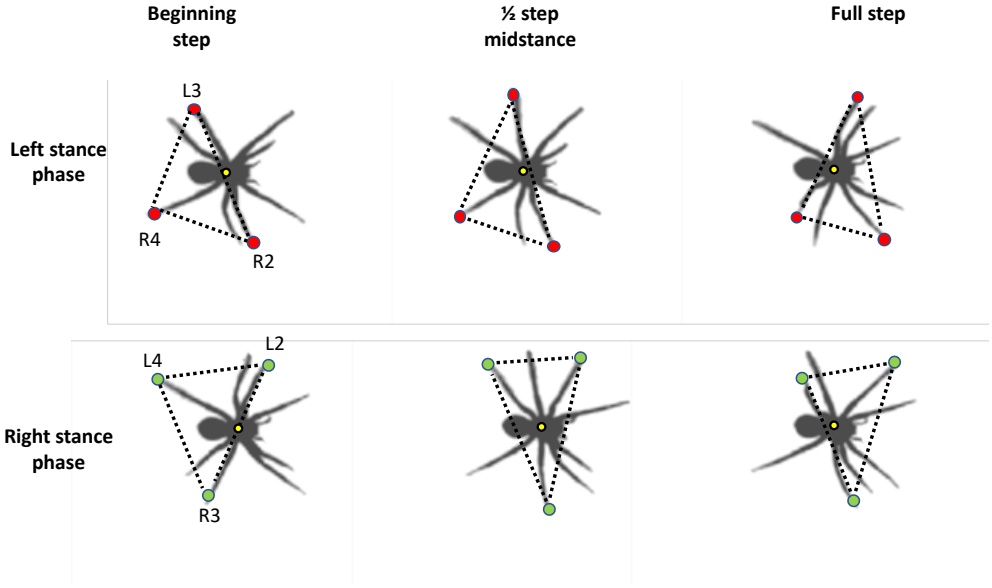

A.9 :Alternating tripod gait of *Dolomedes aquaticus* from a dorsal perspective.
Two-dimensional dynamics of a walking spider, separate into three-legged tripods. Yellow dots demark the center of mass of the spider and coloured dots (red and green) follow the trajectory of moving tripods through one step period. L3: Left-side third leg, R2: Right-side second leg, and R4: Right-side fourth leg correspond to one moving tripod while the other unmarked legs, aside from the front left and right first legs, stay stationary.

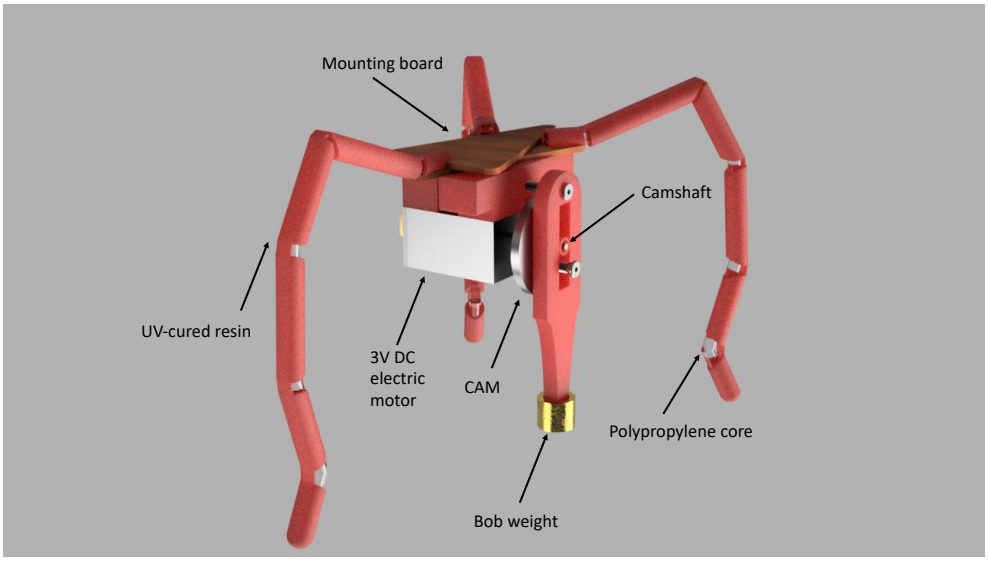

A.10 : Illustration of the tripod model.
The tripod model was used to demonstrate how the pendulum-like movement of a bobweight could be paired with the swinging oscillations of a set of tripod legs. Leg models were reduced and printed on the Anycubic 3D printer in red photoresin. Each leg was hollowed out using a 2mm hand drill. A polypropylene filament was threaded through the leg to make it more flexible. A 3V DC micro electric motor drives an inverted pendulum comprised of a cam with an attached arm and. All three legs were mounted on a wooden mounting board. The total model is 135mm long.

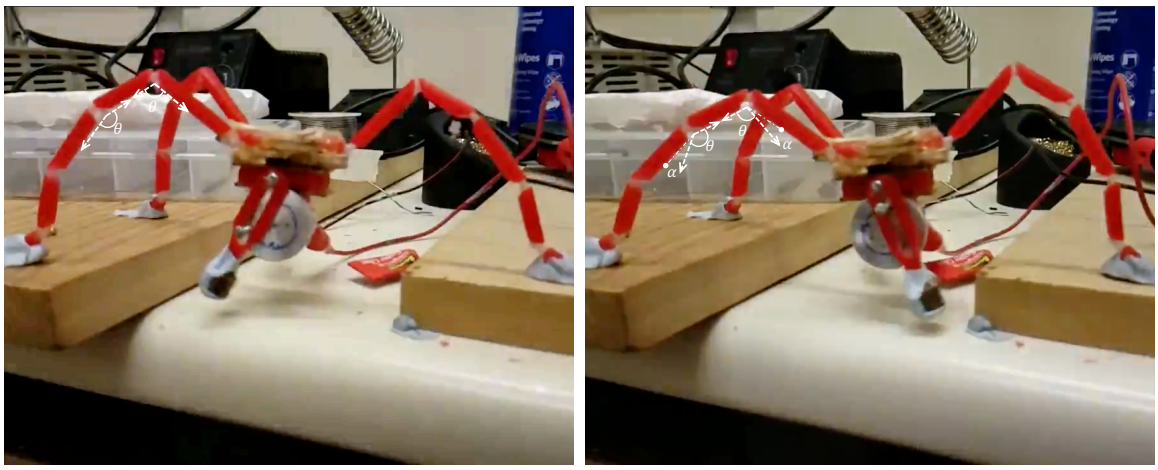

(a) (b)

A.11 : Lateral oscillations of the tripod model.
Joint angle (θ) of the femur-patella and tibia-patella joints are initially measured at the height of the pendulum swing on the left-hand side. As the pendulum swings from left to right, the leg compresses and the new angle of both joints are recorded. The difference between the two legs is demarked by α. Similar joint angle change from compression to extension is measured for the individual leg on the right-hand side of the tripod. On the left-hand side of the model, the observed overall angle change of the femur-patella joint was 5.31 ° ,and the tibia-patella joint 6.41 °. On the right hands side of the model, the angle of the femur-patella joint shifted by 10.39° and the tibia-patella joint shifts by 1.4° from a compressed to extended phase.

A.12 :Total travel of inverted pendulum.
Superimposed semitransparent shots of both left and right peak amplitudes of the pendulum swing period. The total angle of swing travel (θ) is 46.67 °. The dotted black line represents the motion of travel of the pendulum. White dots demark the change in center of mass (COM) from its left maximum position to its right maximum position. The center of mass shifted over a distance of 10.87mm during a given period with a 2.5mm height drop from left to right. This drop in height should have been recovered at the end of the period with a net height drop of 0 mm, (i.e. PE=KE=PE). The shortened pendulum period, and the consequent lack of recovery of the energy could be in part due to the revolving pendulum design. Because the left-hand side of the model is supported by two legs, it does not depress and contract as much compared to the right-hand side because of the added support.